energies

MDPI

Article

Thermal and Thermo-Hydraulic Performance of a Semi-Circular Solar Air Collector Utilizing an Innovative Configuration of Metal Foams

Basim A. R. Al-Bakri [1,*], Ali M. Rasham [2] and Ali O. Al-Sulttani [3]

[1] Department of Aeronautical Engineering, College of Engineering, University of Baghdad, Al-Jadriya Campus, Baghdad 10071, Iraq
[2] Department of Energy Engineering, College of Engineering, University of Baghdad, Al-Jadriya Campus, Baghdad 10071, Iraq; a.rasham@coeng.uobaghdad.edu.iq
[3] Department of Water Resources Engineering, College of Engineering, University of Baghdad, Al-Jadriya Campus, Baghdad 10071, Iraq; ali2003ena@uobaghdad.edu.iq
* Correspondence: b.rasheed@coeng.uobaghdad.edu.iq

Abstract: The enhancement of the thermal and thermo-hydraulic performance of a semi-circular solar air collector (SCSAC) is numerically investigated using porous semi-circular obstacles made of metal foam with and without longitudinal porous Y-shaped fins. Two 10 and 40 PPI porous material samples are examined. Three-dimensional models are built to simulate the performance of SCSAC: model (I) with clear air passage; model (II) with only metal foam obstacles, and model (III) with metal foam obstacles as well as porous Y-fins. COMSOL Multiphysics software version 6.2 based on finite element methodology is employed. A conjugate heat transfer with a (k-ε) turbulence model is selected to simulate both heat transfer and fluid flow across the entire computational domain. However, only the local thermal non-equilibrium (LTNE) model of heat transfer is applied in the porous regions. The findings demonstrated that adding metal foam as the novel proposed configuration particularity of model (III) may enhance the thermal efficiency by about 30%, and the outlet air temperature may rise to 7% compared to other models. Also, the performance evaluation factor of this model is greater than one in all cases. Additionally, the thermal enhancement is accomplished by occupying only 5% of the air passage volume, thereby including an associated pressure drop of minimal magnitude.

Keywords: solar air collector; metal foams; semi-circular; computational fluid dynamics analysis; thermal performance enhancement; heat transfer augmentation

check for updates

Academic Editor: Anastassios M. Stamatelos

Received: 11 April 2025
Revised: 3 May 2025
Accepted: 8 May 2025
Published: 13 May 2025

Citation: Al-Bakri, B.A.R.; Rasham, A.M.; Al-Sulttani, A.O. Thermal and Thermo-Hydraulic Performance of a Semi-Circular Solar Air Collector Utilizing an Innovative Configuration of Metal Foams. *Energies* **2025**, *18*, 2501. https://doi.org/10.3390/en18102501

Copyright: © 2025 by the authors. Licensee MDPI, Basel, Switzerland. This article is an open access article distributed under the terms and conditions of the Creative Commons Attribution (CC BY) license (https://creativecommons.org/licenses/by/4.0/).

1. Introduction

Solar air collectors (SACs) are a flexible technology that plays a crucial part in the shift to a future with more sustainable and renewable energy as a key weapon in the battle against climate change. The SACs can be used for a wide range of applications, including space heating, ventilation in residential and commercial buildings, and even drying crops and other agricultural products due to their efficiency and cost-effectiveness. As a renewable source of heating and ventilation, SACs may be incorporated into existing buildings to save energy costs and increase energy efficiency, which eliminates or reduces the need for conventional heating and cooling systems. The performance and significance of thermal solar collectors were extensively investigated in previous practical, analytical, and computational studies.

Ref. [1] utilized unique pin fin structures to analyze the thermal performance of single-pass, double-pass, and triple-pass solar air heaters. An advantage of pin fins over longitudinal fins has been identified in terms of the highest thermal performance. Steady-state three-dimensional numerical models were developed by [2] to predict the thermal-hydraulic performance for both longitudinal and transverse flow directions through the serrated fins. A thorough description of the local and average heat transfer properties of the two types of serrated fins was provided and discussed. Ref. [3] conducted an experimental study to determine the thermal efficiency of a solar air heater with wavy fins under various operation conditions. Based on mass flow rate and fin spacing, the temperature rise and highest efficiency were estimated. An experimental study on a double-pass converging finned wire mesh-packed bed solar air heater with double glazing was conducted by [4]. The performance was enhanced by utilizing ten layers of wire mesh screens formed between sixteen fins at an appropriate angle in the middle channel. The performance of a double-flow solar air heater roughened with different ribs of varied pitch distance and angle of attack was investigated experimentally by [5]. Compared to other arrangements, superior heat transfer via several C-shaped ribs was realized.

Through the use of longitudinal fins at different heights for entry, ref. [6] experimentally enhanced the performance of a single-pass solar air heater. For the ranges of mass flow rates, the entrance area modification resulted in a considerable improvement in both the output temperature and efficiency. Ref. [7] applied the energy balance technique to numerically simulate the performance of a solar air collector utilizing twisted tape. The highest improvement in performance was achieved for the tape with the lowest twist ratio. The performance of the new double-pass solar air heater with and without aluminum cans in aligned and staggered layouts was experimentally investigated by [8]. The results demonstrated that a staggered arrangement of aluminum cans achieved maximum daily efficiency. Since the absorber plate is the most important component of a thermal solar air collector, a variety of designs were proposed and their effects on performance were demonstrated in previous literature. Ref. [9] investigated how the various amplitudes and wavelengths of wavy fins affected the performance of a single-pass solar air heater. The results showed a considerable improvement in both thermal and thermohydraulic performance involving wavy fins.

The performance of a solar drying system with two cross-matrix absorber solar collectors in parallel and series configurations was experimentally studied by [10]. Under various operating conditions, the parallel configuration showed promising findings in terms of reduced energy use and drying efficiency. Ref. [11] studied the performance of a solar air heater (SAH) with a V-grooved absorber plate over a broad range of operating conditions. The results demonstrated that the performance of double-pass counterflow SAH outperformed the double-parallel flow SAH. Ref. [12] investigated the experimental performance of three solar air collectors including perforated absorber plates in Baghdad, Iraq. The maximum thermal efficiency values were 67%, 64%, and 56% for the solar collector with 3 mm holes, 6 mm holes, and without perforations, respectively. Ref. [13] conducted a numerical analysis of a double-pass solar air heater using finite element methodology via COMSOL Multiphysics software. The average percentage error between the FEM simulation and experimental outcomes was below 1% for both outlet air temperature and thermal efficiency.

The flat and V-corrugated absorber plate solar air heaters with integrated PCM were experimentally studied by [14] in Tanta City, Egypt. Under prevailing environmental conditions, the V-grooved absorber plate improved the daily efficiency and outlet air temperature. Energy, exergy, economic, and environmental evaluations for solar air collectors (SACs) with smooth and V-groove absorber plates were experimentally explored [15]. Despite

having almost higher costs and friction factors, V-groove SACs yield higher heat transfer coefficients. The thermal performance of solar air heaters (SAHs) coupled with winglet vortex generators (WVGs) was numerically enhanced for Reynolds numbers ranging from 3500 to 16,000 [16]. The best thermal enhancement factor was generated for WVGs with a tip edge ratio of $(c/a = 1)$, and an angle of attack of $(\alpha = 30^\circ)$. Ref. [17] conducted an experimental comparison among four different types of dual-channel solar air collectors with traditional ones of smooth absorber plates. Compared with collectors of smooth and wire mesh absorber plates, the solar collector of the perforated V-grooved absorber plate showed the highest energetic and exergetic efficiency.

Ref. [18] utilized an RNG turbulence model to simulate the thermal-hydrodynamic behavior of a three-dimensional circular inclined roof solar air collector. The findings revealed that warm airflow could be produced in Baghdad to provide electricity. Ref. [19] experimentally compared the thermal performance of a zigzag solar air heater with and without steel wire mesh on the absorber plate of the collector under Baghdad climatic conditions. At 45° of inclination, the maximum efficiency was found, and a correlation for the Nusselt number was also established. In earlier literature, the impact of employing porous medium and wire mesh with solar air collectors was investigated to improve performance through increased heat transmission. Ref. [20] improved the performance of a solar water collector using multiple-foam blocks (MFBs). The findings indicate that the MFBs' recirculation would significantly increase the rate of heat transfer. A study conducted by [21] employed eight copper metal foam blocks to numerically investigate the performance of a flat plate solar water collector. The findings show that a drop in the absorber plate temperature and an increase in the heat transfer coefficient of more than 80% led the outlet water temperature to rise. In another study, the same authors [22] discussed the benefit factor of a solar water collector. The benefit factor was less than one due to the 153% increase in pressure drop caused by the use of metal foams. The performance of a porous serpentine wavy wire mesh-packed bed solar air heater was studied experimentally and numerically by [23] for a range of porosity, amplitude, wavelength, and mass flow rate. The optimal arrangement was determined, and it showed that the absorbent SAH with a serpentine-packed bed was superior compared with those having a flat-packed bed. The thermohydraulic performance of a solar air heater with herringbone metal foam fins mounted underneath the absorber plate was experimentally examined [24]. In real outdoor weather conditions, the lowest corrugation angle yielded the highest thermal performance.

Ref. [25] presented a novel solar air heater (SAH) that included a porous absorber plate for the analysis of indirect solar dryer systems. Improved SAH designs have a significant impact on improving thermal performance and efficiency in solar dryer systems. A variety of solar air collector configurations have been studied in earlier articles of literature because a cost-effective solar air heater requires a suitable design for solar energy applications. The thermal performance of a Trapezoid solar air heater was experimentally studied by [26] for utilizing gravel as a heat storage medium in a corrugated absorber plate (TSAHWGs). With TSAHWGs, the highest possible energy efficiency of 12.56 percent was achieved. Ref. [27] proposed constructing a curved-slope solar collector (SSC) on a mountain slope to improve the efficiency of solar chimney power generation. Concerning horizontal and vertical solar collectors, the optimal construction, maximum annual total solar radiation, and slope angle were evaluated. The performance of a honeycomb solar air collector (SAC) paired with photovoltaic modules to provide air circulation from an electric fan was studied experimentally and numerically [28]. Throughout the entire set of testing conditions, the highest instantaneous efficiency was 64% with a PV coverage ratio of 45%.

Ref. [29] conducted an experimental study in Biskra, Algeria, to investigate the performance of a slightly curved solar air heater with a convex absorber plate. Under similar

operating conditions, the total efficiency of solar air heaters is significantly greater than that of traditional ones. Ref. [30] investigated a single-pass gridded solar air heater with a triangle corrugation pattern constructed from six layers of blackened aluminum grid absorbers. An 80% conversion efficiency was identified at a mass flow rate of 0.06 kg/s. A triangular channel performance analysis of a double-pass solar air heater (SAH) with a helical flow path was carried out by [31] utilizing both computational and experimental assessment. At 0.026 kg/s, the thermal efficiency for an SAH with helical channeling is 8.6% and 14.7% higher compared to a finned and a typical duct.

Through experimental research, [32] investigated the thermal performance of a spiral solar air heater (SSAH). Compared to the conventional and serpentine SAH, this type of solar air heater showed superior heat-collecting efficiency. The performance of a new perforated corrugated absorber plate (PCA)-equipped flat plate solar air collector and triangular solar air collector (TSAC) with tilt angles of 60° and 75° was compared experimentally [33]. The most efficient collector among the offered ones was the TSAC with a 60° tilt angle. Ref. [34] presented analytical and numerical investigations of the thermal and thermohydraulic performance of a solar air heater (SAH) with semicircular and triangular ducts. The results demonstrated that the SAH of the semicircular duct, both with and without recycling, outperformed the SAH of the triangular duct. Ref. [35] examined the performance of a double slope solar still integrated with rubber scrapers in regions located near the equator, focusing on the effect of different scraper movement frequencies on hourly water production. Key model parameters, including a constant and an exponent in the Nusselt number equation, were optimized using particle swarm optimization to enhance prediction accuracy. The proposed model demonstrated superior performance with a relative root mean square error of 2.81, which was substantially lower than that of existing models, indicating its reliability in estimating water yield. Ref. [36] developd a two-phase particle flow model using lattice Boltzmann, discrete element, and large eddy simulation methods to analyze mixing and particle behavior in serpentine microchannels. Ultrasonic excitation significantly improved particle dispersion and preventd agglomeration. The findings offered key insights into enhancing mass transfer and optimizing microfluidic chip performance. Ref. [37] developed a model based on computational fluid dynamics and the discrete element method to control particle flow in microreactors using ultrasonic excitation, enhancing mixing and reducing agglomeration. Fractal analysis quantified particle distribution, and a validation platform confirmed simulation accuracy. Key findings showd that ultrasound and flow rate significantly improved particle uniformity and mixing efficiency. Ref. [38] optimized a liquid cooling plate with porous media for lithium-ion battery thermal management using Response Surface Methodology (RSM), Non-dominated Sorting Genetic Algorithm II (NSGA-II), and the Technique for Order of Preference by Similarity to Ideal Solution (TOPSIS). Key variables included porosity, filling ratio, and inlet velocity, targeting temperature control and pressure drop, and the optimal setup achieved balanced thermal performance with a low max temperature 31.29 °C and moderate pressure drop 30,029.89 Pa. Ref. [39] compared liquid cooling plates with and without porous media for lithium-ion battery thermal management, showing superior temperature control with fully filled porous structures. High porosity and thermal conductivity materials significantly reduced cell temperature and enhanced cooling efficiency. Pressure drop was also influenced by porosity, guiding material selection. Ref. [40] modeled a phase-change heat storage unit to enhance solar–biogas heating systems, focusing on heat release under rotation. The optimized design (Model A1) significantly reduced solidification time and boosted efficiency. A Tactical Unit Algorithm helpd achieve supply–demand balance, with economic benefits and ~100 t CO_2 emissions reduction.

To the best of the authors' knowledge, the adaptation of the present innovative configuration of a semicircular air collector featuring an absorber plate with the same geometry, which is partially filled with semicircular metal foam obstacles, and is integrated with porous Y-fins along the air passage duct, has not been explored in existing literature. The main objective of the current study is to improve the thermal performance of the proposed systems to achieve a performance evaluation factor exceeding one. The enhancement of thermal performance in solar air collectors using a low filling ratio and a unique configuration has been sufficiently explored, effectively addressing the issue of high convective thermal resistance in traditional planar structures. The key research features in this field can be described as follows:

1. This study develops a detailed three-dimensional model of the SCSAC using the COMSOL Multiphysics software version 6.2, including many operational and geometrical parameters, such as solar irradiation, ambient temperature, wind speed, SCSAC dimensions, and metal foam materials with different specifications. The methodology employed for heat generation within metal foams was originally developed and formulated by the authors.
2. The influence of the configuration and distribution of metal foams in air ducts on thermal performance was studied. The purpose of utilizing semicircular metal foam obstacles is to inhibit the development of the thermal boundary layer, hence enhancing the heat transfer coefficient. Additionally, the purpose of employing Y-shaped metal foam fins is to induce turbulence, hence improving the heat transfer coefficient. Accordingly, the thermal performance will be improved.

2. Methodology

2.1. Geometry and System Description

Figure 1 shows the SCSAC with and without the metal foams assembly under discussion. It involves an aluminum container containing a semicircular absorber plate integrated with semicircular obstacles and Y-shaped fins of aluminum metal foams. The specifications of SCSAC are shown in Table 1 [41]. Table 2 displays the thermo-physical properties and specifications of the metal foams used in the current study [42]. In the case of combining the porous Y-fins with porous semicircular obstacles as a novel construction, the investigation of the thermal performance of the SCSAC was employed.

The enhanced thermal conductivity, lower cost, light weight, and high surface area density of the metal foam materials are the key choice criteria. The semicircular absorber plate integrated with porous Y-fins and semicircular obstacles of metal foams behaves as a heat source. The heat dissipated inside the absorber plate is transferred through Y-fins and semicircular obstacles of metal foams by conduction, and convection with the forced air in the duct. Conduction and convection work together to transfer heat within the foam metallic ligaments and through the air in the pores. The driven air inside the duct is heated by this combined heat transfer process. Generally, the bottom surface and side edges typically lose heat through conduction, convection, and radiation. The heat losses by radiation are disregarded for small temperature differences between the ground surface and the back surface of the SCSAC system. Based on the value of wind velocity, the convection heat losses from the top and bottom surfaces of the SCSAC are depicted.

(**a**)

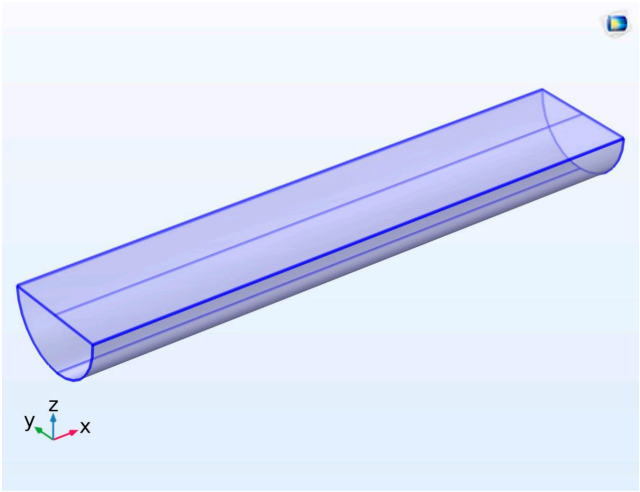

(**b**)

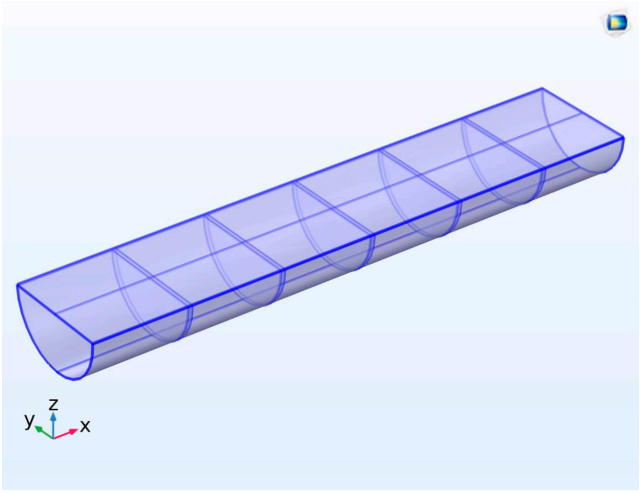

(**c**)

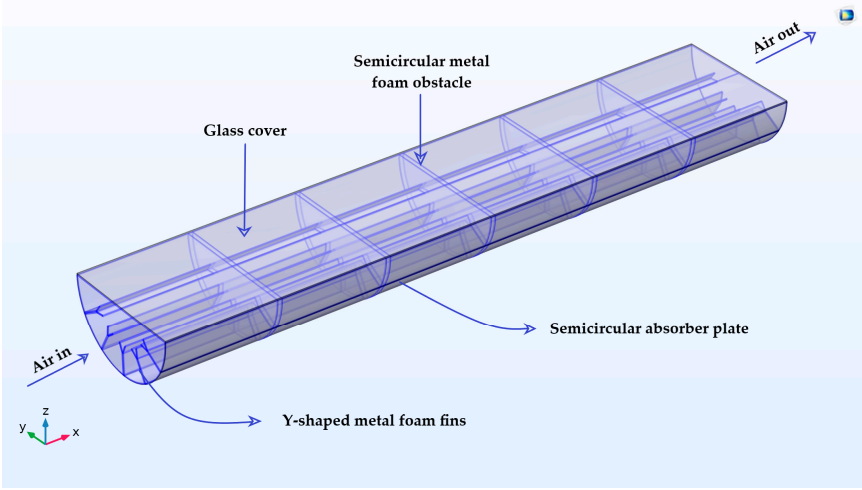

Figure 1. Schematic of SCSAC: (**a**) without metal foams, (**b**) with semicircular obstacles of metal foams, and (**c**) Y-fins and semicircular obstacles of metal foams.

Table 1. Specifications of SCSAC [41].

System and Operating Parameters	Value
Collector length (L_{sc})	1.5 ⟨m⟩
Collector width (diameter) (W_{sc})	0.3 ⟨m⟩
Number of Y-shaped fins (n)	5 ⟨−⟩

Table 1. *Cont.*

System and Operating Parameters	Value
Fin height (H_f)	0.05 ⟨m⟩
Fin thickness (t_f)	0.003 ⟨m⟩
Thickness of absorber plate, (t_p)	0.001 ⟨m⟩
Fin distribution angles $(\theta = 180/[n+1])$	30°
Thermal conductivity of absorber plate (k_{ab})	238 ⟨W/(m·K)⟩
Thermal conductivity of glass cover (k_g)	1.4 ⟨W/(m·K)⟩
Absorptivity of absorber plate (α_p)	0.95
Absorptivity of glass cover (α_p)	0.05
Emissivity of absorber plate (ϵ_p)	0.94
Emissivity of glass cover (ϵ_g)	0.90
Transmissivity of glass cover (τ_g)	0.875
The intensity of solar radiation reaching the SCSAC (I_s)	750 $\langle W/m^2 \rangle$
Ambient temperature (T_a)	25 ⟨°C⟩
Wind speed (V_w)	1 ⟨m/s⟩

Table 2. Specifications of aluminum metal foams [42].

MF Samples	Thermal Conductivity (W/m·°C)	Density (kg/m^3)	Heat Capacity (J/kg·°C)	Pore Density (1/m)	Porosity (%)	Permeability ($\times 10^7$ m^2)	Forchheimer Coefficient (−)
1	238	2700	900	10	90.85	1.62	0.078
2				40	95.85	0.54	0.086

2.2. System Modelling

The system modeling of the proposed solar air collector configuration incorporates fluid dynamics models to assess airflow and heat transfer models to evaluate energy conversion. These models simulate overall system behavior under different operating conditions, providing insights into its behavior and efficiency.

2.2.1. Fluid Flow Model

Fluid flow in the free and porous regions was modeled utilizing the free and porous media flow model. The non-Darcian flow model was employed where the inertial effect is included. The Navier–Stokes equations in the free regions and Forchheimer–Brinkman–Darcy extended equations in the porous regions are represented in this software. The coupling of these two sets of equations is solved at the interface surfaces via the continuity of velocity, pressure, stresses, turbulent kinetic energy, and turbulent dissipation rate. The entrance length effect is taken into account within the COMSOL Multiphysics simulation environment, indicating that the flow is not presumed to be fully developed at the inlet. This effect is incorporated into the computational domain and is consequently reflected in the overall analysis and results of the study. The mass flow rates utilized in this study were 0.01, 0.03, 0.05, 0.07, 0.09, and 0.11 (kg/s), respectively. The Reynolds numbers associated with these mass flow rates at the entrance of the semicircular duct were 2823.3, 8470, 14,117, 19,763, 25,410, and 31,507, respectively. Consequently, the flow regimes transitioned from transitional to fully turbulent flow. The current study employed turbulent flow to simulate the fluid flow model, informed by the Reynolds number values and the existence of metal

foam obstacles. The Reynolds-averaged Navier–Stokes (RANS) turbulence model was adopted. COMSOL Multiphysics software version 6.2 incorporates a suite of two-equation turbulence models, which were effectively employed to characterize airflow behavior within the fluid domains across a range of operating conditions. To accurately model airflow in the porous region, the (κ–ε) turbulence model was adopted, as recommended in [41]. This approach ensured consistency and continuity in turbulence representation between the free-flow and porous regions. The production of turbulent kinetic energy due to the gradient in the flow velocity was added to the governing equations. Also, the generation rate of turbulent kinetic energy and turbulent dissipation due to the action of the porous matrix was added to the governing equations.

2.2.2. Heat Transfer Model

Heat transfer in the fluid and solid domains was modeled via the conjugate heat transfer model. Additionally, heat transfer in the porous media model was added to the conjugate heat transfer model to simulate heat transmission in the porous regions. Based on the local thermal non-equilibrium model (LTNE), two-energy equations for the fluid and porous matrix of porous medium were utilized. The heat generated in the absorber plate and porous matrix of the porous medium was included in the energy equations as a heat source. The continuity of temperature and heat flux at interface surfaces between the free and porous regions was adopted. The Kays–Crawford heat transport turbulence model with a standard thermal wall function was used to model the turbulent thermal boundary layer. Based on the Ray shooting method, a surface-to-surface radiation heat transfer model was used to simulate the radiation heat transfer within the semicircular duct of a semicircular solar air collector. Convection and radiation heat losses from the glass layer to the ambient air were considered. The minimal temperature difference between the solar collector's bottom plate and the ground surface allowed for the disregard of radiation heat losses.

2.3. Mathematical Model

The numerical solution can be achieved by applying a few simplifying assumptions. These are as follows:

(a) Steady-state incompressible flow.
(b) The flow analysis covers entrance and fully developed regions.
(c) The flow is modeled as turbulent flow because of the following:
    - The obstruction of metal foam.
    - The Reynolds numbers at the entrance of the air passage are mostly in the turbulent region.
(d) The thermo-physical properties of the working fluid (air) are constant.
(e) The properties of metal foams are uniform, homogeneous, and isotropic.
(f) The bottom and side edges are well-insulated.
(g) The radiation heat losses from the bottom side are neglected.
(h) There is no air leakage.

2.3.1. Energy Balance Technique of SCSAC System

The energy balance for the glass cover is written as follows [43]:

$$-\lambda_g\left(\partial T_g/\partial n\right) = I_s \times \alpha_g - h_{co}\left(T_g - T_{amb}\right) - \epsilon_g \sigma F_s\left(T_g^4 - T_{sk}^4\right) \quad (1)$$

Equation (1) represents the heat absorbed and heat lost by the convection and radiation of the glass cover.

Here, the sky temperature and combined convective heat transfer coefficient (HTC) can be expressed respectively as

$$T_{sk} = 0.0552\, T_{amb}^{1.5} \tag{2}$$

$$h_{co} = h_{fc} + h_{nc} \tag{3}$$

The forced and natural convection heat transfer coefficients can be written as follows [43]:

$$h_{fc} = \begin{cases} 2\frac{\lambda_a}{L_{sc}} \frac{0.3387 Pr^{1/3} Re_L^{1/2}}{\left\langle 1+(0.0468/Pr)^{2/3} \right\rangle^{1/4}} \text{ if } Re_L \leq 5\times 10^5 \\ 2\frac{\lambda_a}{L_{sc}} Pr^{1/3} \left\langle 0.037 Re_L^{4/5} - 871 \right\rangle \text{ if } Re_L > 5\times 10^5 \end{cases} \tag{4}$$

$$h_{nc} = \begin{cases} \frac{\lambda_a}{L_c} \left[0.68 + \frac{0.67 \langle \cos(\beta) Ra_L \rangle^{1/4}}{\left\langle 1+(0.492/Pr)^{9/16} \right\rangle^{4/9}} \right] \text{ if } Ra_L \leq 10^9 \\ \frac{\lambda_a}{L_c} \left[0.825 + \frac{0.387 \langle Ra_L \rangle^{1/6}}{\left\langle 1+(0.492/Pr)^{9/16} \right\rangle^{8/27}} \right] \text{ if } Ra_L > 10^9 \end{cases} \tag{5}$$

The shape factor of radiation heat transfer can be computed as

$$F_s = [1 \mp \cos(\beta)]/2 \tag{6}$$

Equations (2)–(6) are related to equation (1) to evaluate its parameters. Together, they are used to simulate the heat balance on the glass cover of the collector, forming an integral part of the simulation process.

2.3.2. Governing Equations in Free and Porous Regions

The system for governing equations for the airflow model was given by Equations (7)–(17) [44]. The conservation laws for the airflow inside the porous media and free regions inside the air duct of the SCSAC system are expressed as

$$\nabla \cdot \left(\rho \vec{V} \right) = 0 \tag{7}$$

$$\frac{\rho}{\varnothing_p} \left(\langle \vec{V} \cdot \nabla \rangle \frac{\vec{V}}{\varnothing_p} \right) = -\nabla \cdot \left[\langle p \rangle^i I + K \right] - \left\{ \frac{\mu}{\kappa} + \rho \frac{C_F}{\sqrt{\kappa}} \langle \vec{V} \rangle^i \right\} \langle \vec{V} \rangle^i \tag{8}$$

The momentum equation in the free regions of the air duct can be derived from Equation (8), by putting $(\varnothing_p = 1)$ and $(\kappa \sim \infty)$ in the right-hand side.

The viscous stress tensor can be expressed as

$$K = (\mu + \mu_T) \left(\nabla \langle \vec{V} \rangle^i + \left(\nabla \langle \vec{V} \rangle^i \right)^T \right) \tag{9}$$

The turbulent kinetic energy (TKE) and turbulent dissipation rate (TDR) for porous medium are written as

$$\rho \left(\vec{V} \cdot \nabla \right) \frac{\langle k \rangle^i}{\varnothing_p} = \nabla \cdot \left[\left(\mu + \frac{\mu_T}{\sigma_k} \right) \nabla \langle k \rangle^i \right] + \mathcal{P}_k + \mathcal{P}_{k,pm} - \rho \varepsilon \tag{10}$$

$$\rho \left(\vec{V} \cdot \nabla \right) \frac{\langle \varepsilon \rangle^i}{\varnothing_p} = \nabla \cdot \left[\left(\mu + \frac{\mu_T}{\sigma_\varepsilon} \right) \nabla \langle \varepsilon \rangle^i \right] + C_{\varepsilon 1} \frac{\langle \varepsilon \rangle^i}{\langle k \rangle^i} \mathcal{P}_k + \mathcal{P}_{\varepsilon,pm} - C_{\varepsilon 2} \rho \frac{\langle \varepsilon \rangle^{i2}}{\langle k \rangle^i} \tag{11}$$

whereas the TKE and TDR for free fluid flow regions are written as

$$\rho\left(\vec{V}.\nabla\right)k = \nabla\cdot\left[\left(\mu + \frac{\mu_T}{\sigma_k}\right)\nabla k\right] + \mathcal{P}_k - \rho\varepsilon \tag{12}$$

$$\rho\left(\vec{V}\cdot\nabla\right)\varepsilon = \nabla\cdot\left[\left(\mu + \frac{\mu_T}{\sigma_\varepsilon}\right)\nabla\varepsilon\right] + C_{\varepsilon 1}\frac{\varepsilon}{k}\mathcal{P}_k - C_{\varepsilon 2}\rho\frac{\varepsilon^2}{k} \tag{13}$$

where $\left(\mathcal{P}_{k,pm}\right)$, and $\left(\mathcal{P}_{\varepsilon,pm}\right)$ in Equations (9) and (10), can be estimated as

$$\mathcal{P}_{k,pm} = \rho\frac{C_F}{\sqrt{\kappa}}\left|\vec{V}\right|^3 \tag{14}$$

$$\mathcal{P}_{\varepsilon,pm} = C_{\varepsilon 2}\frac{\rho C_{stpm}\left|\vec{V}\right|}{\sqrt{\kappa/\varnothing_p}\varnothing_p}\langle\varepsilon\rangle^i \tag{15}$$

The turbulent eddy viscosity (μ_T) and the production due to mean velocity shear (P_k) are formulated, respectively, as

$$\mu_T = \rho C_\mu\frac{\langle k\rangle^{i2}}{\mu\langle\varepsilon\rangle^i\varnothing_p} \tag{16}$$

$$\mathcal{P}_k = \frac{\mu_T}{\varnothing_p}\left[\nabla\vec{V} : \left(\nabla\vec{V} + \langle\nabla\vec{V}\rangle^T\right)\right] \tag{17}$$

For free fluid regions, the $(\mathcal{P}_k)$ can be derived by putting $(\varnothing_p = 1)$ in Equation (17).

The system of governing equations and related parameters for the heat transfer model is given by Equations (18)–(25) [45]. The energy equations in solid and fluid domains of SCSAC system are written, respectively, as

$$0 = \lambda_s\nabla^2 T + Q_g \tag{18}$$

$$(\rho C_p)_f\left(\vec{V}\cdot\nabla T\right) = \lambda_f\nabla^2 T \tag{19}$$

For local thermal non-equilibrium (LTNE) between porous matrix and fluid in pores, the energy equations of SCSAC system are defined as

$$\left(\rho C_p\right)_f\left(\langle\vec{V}\rangle^i\cdot\nabla\langle T_f\rangle^i\right) = \left(\varnothing_p\lambda_f\right)\nabla^2\langle T_f\rangle^i + h_{sf}A_{sf}\left(\langle T_s\rangle^i - \langle T_f\rangle^i\right) \tag{20}$$

$$\left(1-\varnothing_p\right)\lambda_s\nabla^2\langle T_s\rangle^i + \left(1-\varnothing_p\right)Q_g = h_{sf}A_{sf}\left(\langle T_s\rangle^i - \langle T_f\rangle^i\right) \tag{21}$$

Here, the surface area density, interfacial heat transfer coefficient, and fluid-to-solid Nusselt number are calculated as

$$A_{sf} = 6\left(1-\varnothing_p\right)/d_p \tag{22}$$

$$\left(1/h_{sf}\right) = \left(d_p/\lambda_f Nu\right) + \left(d_p/10\lambda_s\right) \tag{23}$$

$$Nu = 2 + 1.1Pr^{1/3}Re_p^{0.6} \tag{24}$$

The particle Reynolds number can be written as

$$Re_p = \rho_f|u|d_p/\mu \tag{25}$$

The average HTC and Nu along PVT collector can be estimated by [46].

$$\overline{h} = \langle Q_u \rangle / \langle A_{s-ab} (\overline{T}_p - \overline{T}_f) \rangle \tag{26}$$

$$\overline{Nu} = \frac{1}{L} \left[\int_{L_i}^{L_f} (Nu)_x dx \rfloor_{FR|_{i=1}^{N}} + \int_{L_i}^{L_f} (Nu_{sf})_x dx \rfloor_{PR|_{i=1}^{N}} \right] = \langle \overline{h}\, D_h \rangle / \langle k_f \rangle \tag{27}$$

The hydraulic diameter and Reynolds number can be written as

$$D_h = 4A_d / P_w \tag{28}$$

$$Re = (\dot{m} D_h) / A_d \mu \tag{29}$$

2.3.3. Surface-to-Surface Radiation Model

The surface radiosity due to diffusely reflected and emitted radiation is expressed as

$$J = \epsilon_p e_b(T) + \rho_d G \tag{30}$$

The blackbody hemispherical total emissive power can be expressed as

$$e_b(T) = N^2 \sigma T^4 \tag{31}$$

The net radiative heat source can be written as

$$q_{r,net} = \epsilon_p (G - e_b(T)) \tag{32}$$

The equations for surface-to-surface radiation heat transfer (30)–(32) are formulated according to [47].

2.4. Performance Evaluation of SCSAC System

For SCSAC, the useful gains and thermal and thermo-hydraulic efficiencies can be expressed, respectively, as

$$Q_u = \dot{m} C_p (T_o - T_{in}) \tag{33}$$

$$\eta_t = (Q_u) / (I_s A_{sc}) \tag{34}$$

$$\eta_{th} = (Q_u - P_{fn}) / (I_s A_{sc}) \tag{35}$$

The consumption of fan power can be written as

$$P_{fn} = (P_{fl}) / (CF) \tag{36}$$

The pumping power (P_{fl}) of air flowing in the SCSAC system can be expressed as

$$P_{fl} = (\dot{m} \Delta p) / (\rho) \tag{37}$$

The performance evaluation factor (PEF) for the adopted collectors can be expressed as follows [48]:

$$PEF = [Nu \rfloor_{MF} / Nu \rfloor_o] / (\Delta p_{MF} / \Delta p_o)^{(1/3)} \tag{38}$$

Statistical Evaluation of the Studied Parameters with Reference to Model (I)

The evaluation of the enhancement for the proposed filling configurations in a semicircular air passage of model (II) and model (III) can be estimated for each studied parameter compared to the reference model (I) with a clear semicircular air passage as follows:

- Outlet air temperature evaluation can be estimated by calculating the outlet air temperature rise of model (II) and model (III) compared to model (I) as follows:

$$\Delta T_r\rfloor_{II,III} = T_o\rfloor_{II,III} - T_o\rfloor_I \quad (39)$$

- The pressure drop evaluation can be estimated by calculating the additional pressure drop of model (II) and model (III) compared to model (I) as follows:

$$\Delta p_{add}\rfloor_{II,III} = \Delta p\rfloor_{II,III} - \Delta p\rfloor_I \quad (40)$$

- The fan power consumption can be evaluated by calculating the additional fan consumption of model (II) and model (III) compared to model (I) as follows:

$$\Delta P_{fn,add}\rfloor_{II,III} = P_{fn}\rfloor_{II,III} - P_{fn}\rfloor_I \quad (41)$$

- Useful heat gain evaluation can be estimated by calculating the useful heat gain rise of model (II) and model (III) compared to model (I) as follows:

$$\Delta Q_{u,r}\rfloor_{II,III} = Q_u\rfloor_{II,III} - Q_u\rfloor_I \quad (42)$$

- The percentage enhancement of the thermal efficiency of model (II) and model (III) compared to model (I) can be evaluated as follows:

$$\eta_{t,enh}\rfloor_{II,III} = \left[\left(\eta_t\rfloor_{II,III} - \eta_t\rfloor_I\right)/\eta_t\rfloor_I\right] \times 100 \quad (43)$$

- The percentage enhancement of thermo-hydraulic efficiency of model (II) and model (III) compared to model (I) can be evaluated as:

$$\eta_{th,enh}\rfloor_{II,III} = \left[\left(\eta_{th}\rfloor_{II,III} - \eta_{th}\rfloor_I\right)/\eta_{th}\rfloor_I\right] \times 100 \quad (44)$$

These equations are employed as a statistical technique to evaluate the improvements in the examined parameters that have been discussed in detail within the discussion section.

3. Numerical Analysis

3.1. Numerical Solution

Finite element discretization based on the COMSOL Multiphysics software version in 6.2 is used to generate the numerical solution for the SCSAC system with Y-shaped porous fins and porous semicircular obstacles. The problem solution is based on the Galerkin least squares finite element method. The system equations are stabilized consistently using streamlined and crosswind diffusion. For pressure–velocity fields, shape functions of the same second-order interpolation and quadratic Lagrange for temperature discretization were employed. A nonlinear solver based on a modified Newton approach is used to solve all quantities simultaneously. The system of linear equations with stationary solvers that results from utilizing block low-rank factorization with tolerance (10^{-4}) is directly solved using the parallel sparse direct solver (PARDISO). The parameters for a segregated solution method are managed in each sub-step, and employ a damped version of Newton's technique. The segregated iterations are stopped under the control of the termination approach when the estimated relative error is less than a certain tolerance. The convergence requirements for the energy, momentum, and continuity equations were set at (10^{-6}), (10^{-4}), and (10^{-4}) accordingly. The opaque surface-to-surface radiation heat transfer model was utilized to simulate the radiation heat transfer inside the SCSAC duct. The hemicube surface-

to-surface radiation method was selected with 256 radiation resolution. In every nonlinear iteration, the view factor updates the threshold to check the consistency of computation. The Jacobian contribution was determined from local contributions to radiosity. The quadratic discretization of surface radiosity was selected to achieve higher precision.

3.2. Grid Independency

The governing differential equations and the corresponding boundary conditions are solved on a stationary-mesh computational domain. The findings on mesh independence are displayed in Figure 2 at a mass flow rate of 0.01 kg/s. Several element mesh sizes are adopted, from extremely coarse to fine elements of (347,133, 645,345, 1,173,164, 2,261,126, 5,172,181, and 13,669,852) element numbers, respectively. It is obvious that raising the computational domain's cells from a normal mesh does not show any significant variations in the output air temperature. For balancing between good accuracy and computation time, the normal mesh of (5,172,181) elements is selected. Therefore, this mesh has been used for complete simulations.

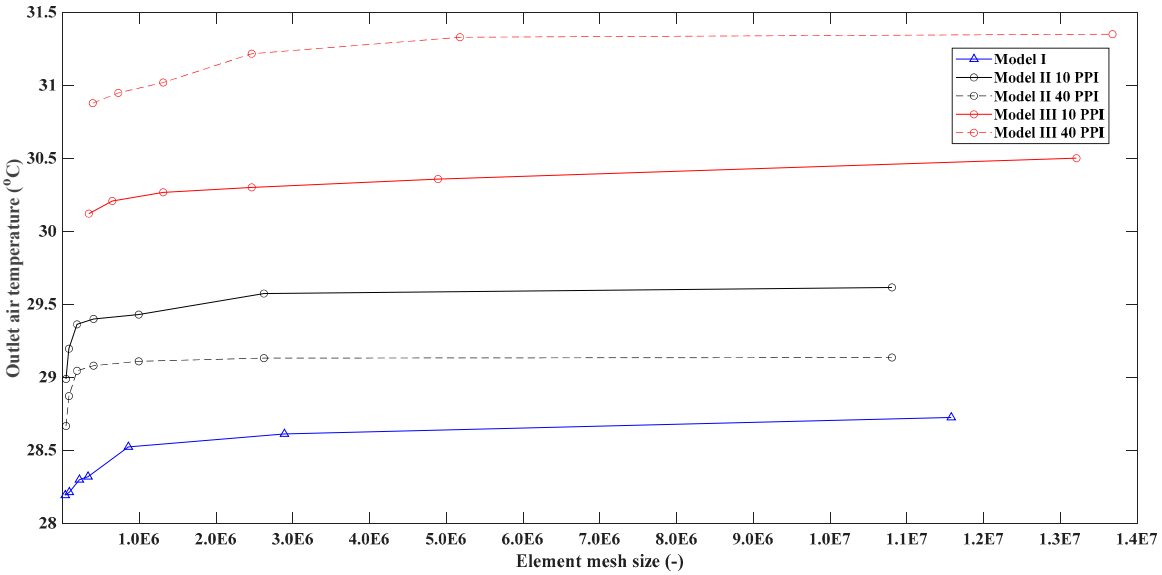

Figure 2. Grid independence of outlet air temperature with element mesh numbers at a mass flow rate of 0.01 kg/s.

3.3. Model Validation

The performance of the SCSAC was previously examined both analytically and computationally by [40], focusing on longitudinal solid fins with rectangular profiles mounted in a semicircular air duct. In this study, a three-dimensional model of the SCSAC is developed using COMSOL Multiphysics software version 6.2, incorporating a combined heat transfer and turbulence modeling approach to evaluate its overall performance. The validation process involves replicating the conditions of the reference study, maintaining consistency in system dimensions, thermo-physical properties of airflow, boundary conditions, and material specifications. To ensure the accuracy of the present model, a series of simulations were performed for SCSAC with longitudinal solid fins (1, 3, and 5) at a mass flow rate of 0.025 kg/s, in accordance with the reference study. Figure 3 presents the temperature contours as cut-planes along the air passage, while Table 3 illustrates the outlet air temperature results for the single-glass, single-pass SCSAC. The absolute relative error values between the predicted values and the findings of the reference study confirm the reliability and accuracy of the developed model in the current study, as shown in Table 3.

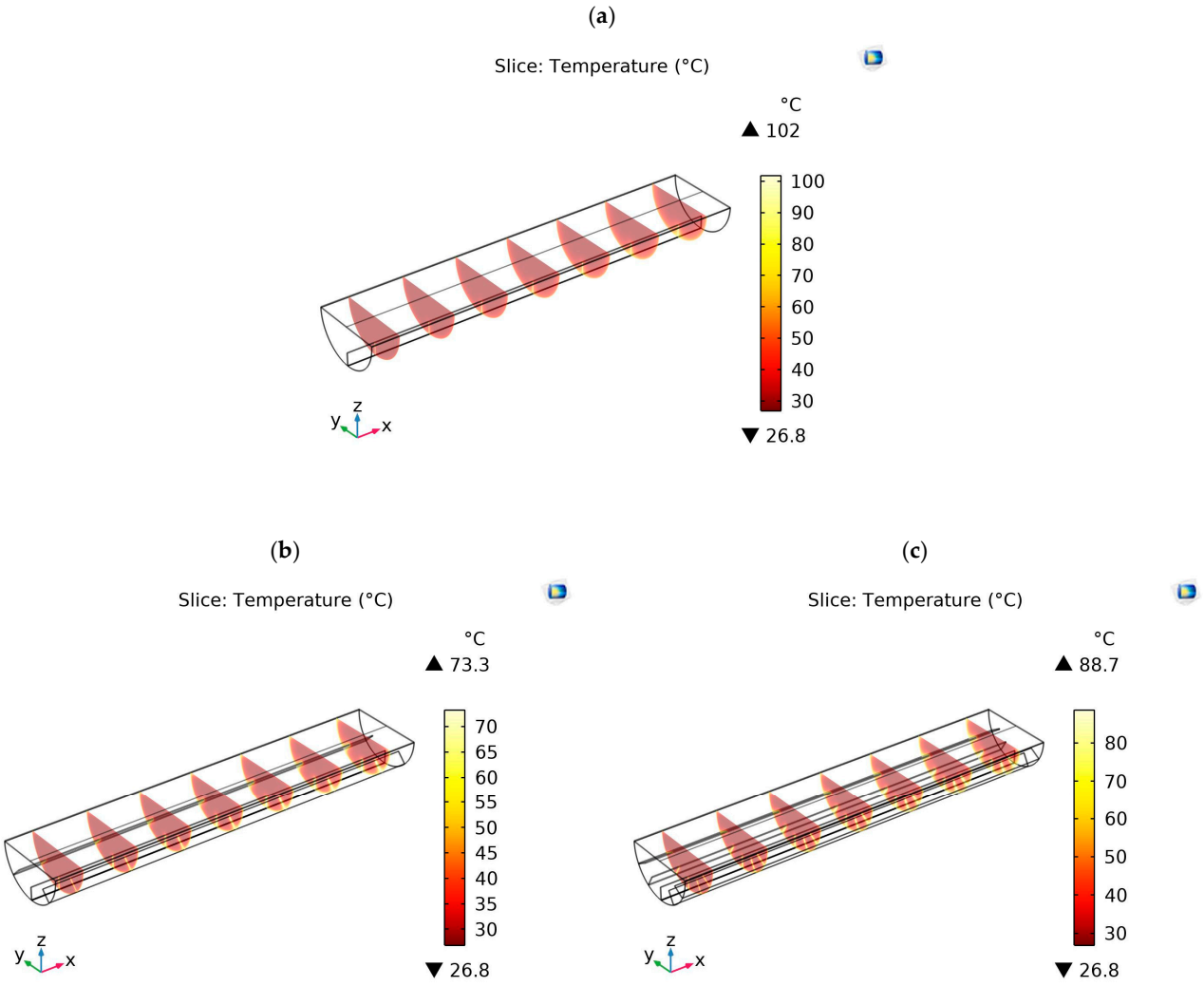

Figure 3. Temperature contours of SCSAC of (**a**) 1 fin, (**b**) 3 fins, and (**c**) 5 fins, for reference [40].

Table 3. Comparison of the present outlet air temperature with reference study [40].

$\dot{m}$ ⟨kg/s⟩	N_{fins}	$E_r\langle\%\rangle=\{\lvert\langle T_o\rangle_{Ref.}-\langle T_o\rangle_{Num.}\rvert/\langle T_o\rangle_{Ref.}\}\times 100$		
		$\langle T_o\rangle_{Ref.}$	$\langle T_o\rangle_{Num.}$	$E_r\langle\%\rangle$
0.025	1	35.3199	36.3060	2.7919
	3	37.6624	36.6460	2.6987
	5	40.1088	41.5210	3.5209

3.4. The Initial and Boundary Conditions

The proposed systems are exposed to the following environmental conditions: solar intensity of 750 W/m^2, ambient temperature of 25 °C, and wind speed of 1 m/s. The adopted mass flow rates were 0.01, 0.03, 0.05, 0.05, 0.07, 0.09, and 0.11 (kg/s). The properties of adopted SCSAC and MF samples were mentioned previously. Table 4 displays the initial and boundary conditions for the fluid flow and heat transfer models.

Table 4. Initial and boundary conditions in the current study.

No.	Section/Condition	Fluid Flow Model	Heat Transfer Model
1	Condition	$V = V_{init}$; $k = k_{init}$; $\varepsilon = \varepsilon_{init}$	$T = T_{init}$
2	Inlet section	$M_f = \dot{m}/A_d$	$T = T_{in} = T_{amb}$
3	Inside face of glass cover	No slip conditions	-
4	Interface surfaces between FR and PR	Continuity of $(V, p, k, \text{and } \varepsilon)$	Continuity of (T) and (q)
5	Outlet section	$\partial k/\partial n = 0$; $\partial \varepsilon/\partial n = 0$; $p = 0$	$\partial T/\partial n = 0$
6	Outside face of glass cover	-	Equation (1)
7	Absorber plate	No slip conditions	$Q_g''' = I_s \tau_g \alpha_{ap}/t_{ap}$
8	Metal foam obstacles	-	$Q_{MF}''' = I_s \tau_g \alpha_{ap} A_{sf}$
9	Bottom plate	Included in (4)	Insulated wall

The methodology adopted for generated heat within the metal foam was originally developed and formulated by the authors and is outlined in point 8 of Table 4.

4. Results and Discussion

Three models, model (I) without metal foams, model (II) with porous obstacles, and model (III) with porous obstacles and fins, were all constructed by using the numerical solution. A mass flow rate range of 0.01–0.11 kg/s and two PPI of 10 and 40 were utilized throughout the solution. The following sections declare the main findings of the current work.

4.1. Velocity Contours

The velocity contours of the proposed designs for SCSAC with mass flow rates of only 0.03, 0.07, and 0.11 kg/s are displayed in Figures 4–6. Generally, the air velocity inside the SCSAC increases as the mass flow rate increases. The findings demonstrated that, for all suggested designs of the SCSAC, the velocities at the walls satisfy the non-slip condition. The air velocity of model (I) increases as it moves away from the walls toward the center of the channel, where the air velocity reaches the peak value. A parabolic velocity profile characterizes the gradual evolution of the velocity boundary layer. The airflow from the collector's inlet section is reduced in velocity by the semicircular metal foam obstacles of model (II). As it leaves the semicircular foam, the air speeds up considerably in the free zones and slows down as it approaches the second foam. Each two successive metal foams have airflow that follows this pattern, except the final metal foam, whose airflow increases as it leaves the channel. Before reaching the semicircular metal foams in model (III), airflow concentrates between the longitudinal Y-shaped porous foams and over their upper portion, which is free of those foams. For models (II) and (III), the results confirm that the 40 PPI MF sample has a lower air velocity than the 10 PPI MF samples because of more airflow resistance. The findings demonstrated that, in comparison to the free zones within the solar collector channel, the air velocity inside the metal foams is the lowest.

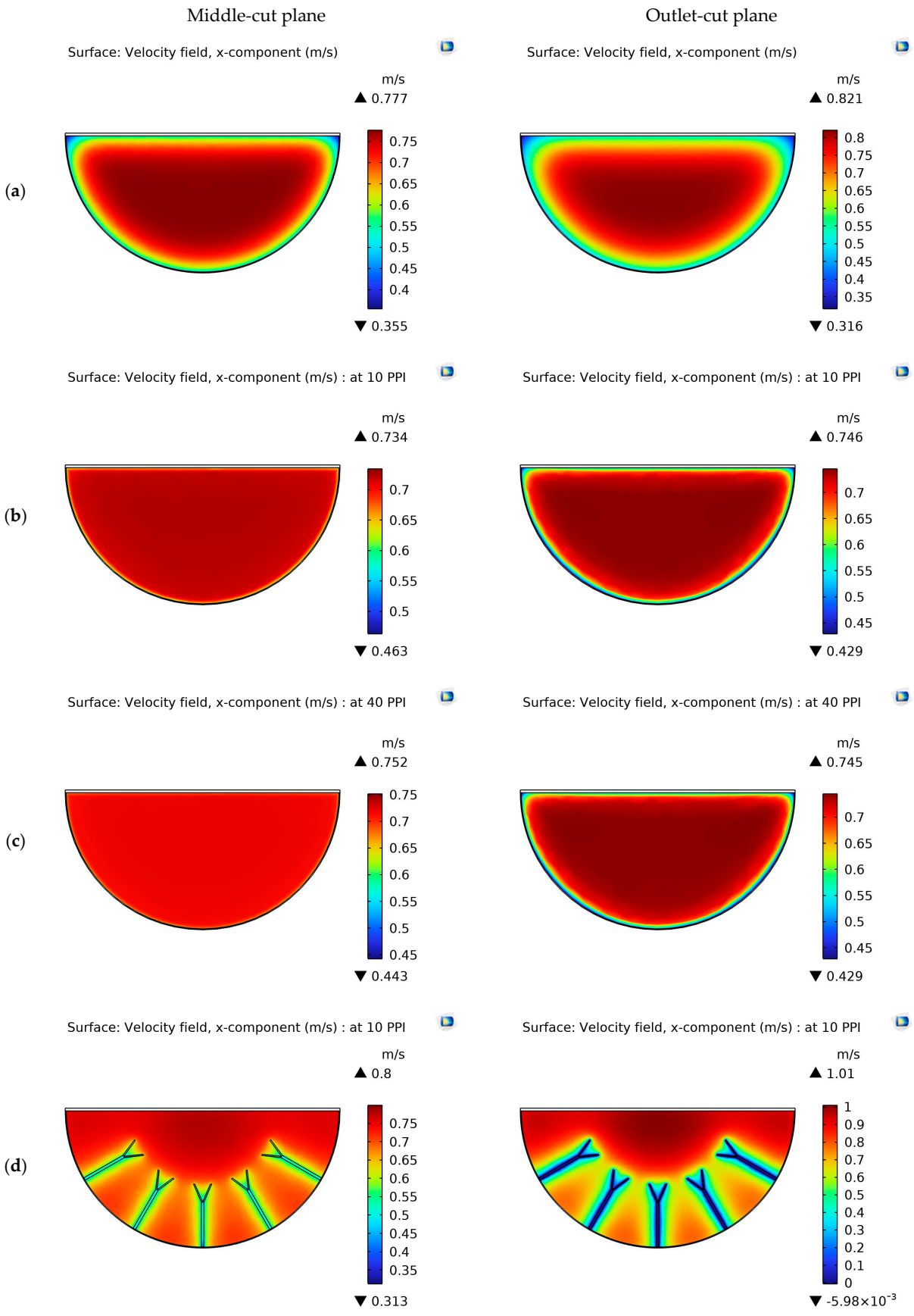

Figure 4. *Cont.*

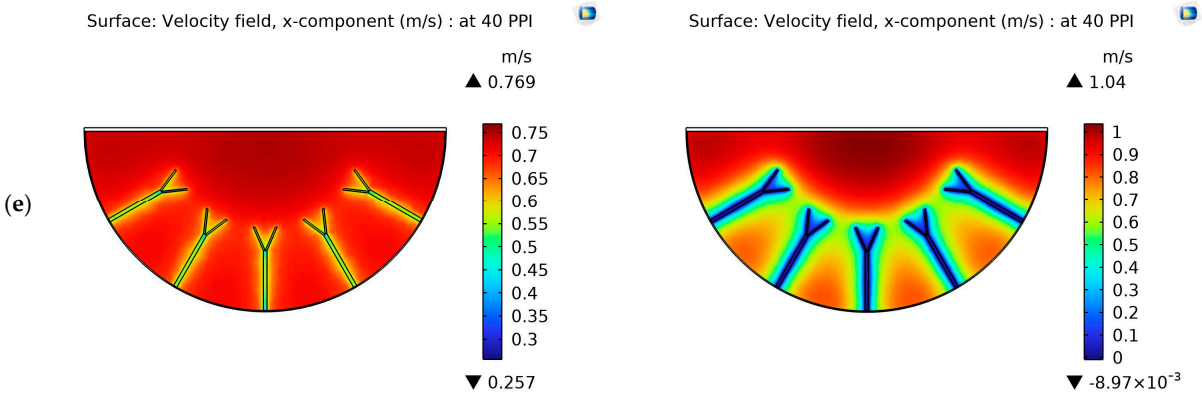

Figure 4. Velocity contours at $\dot{m} = 0.03$ kg/s for (**a**) collector (I), (**b**) collector (II) 10 PPI, (**c**) collector (II) 40 PPI, (**d**) collector (III) 10 PPI, and (**e**) collector (III) 40 PPI.

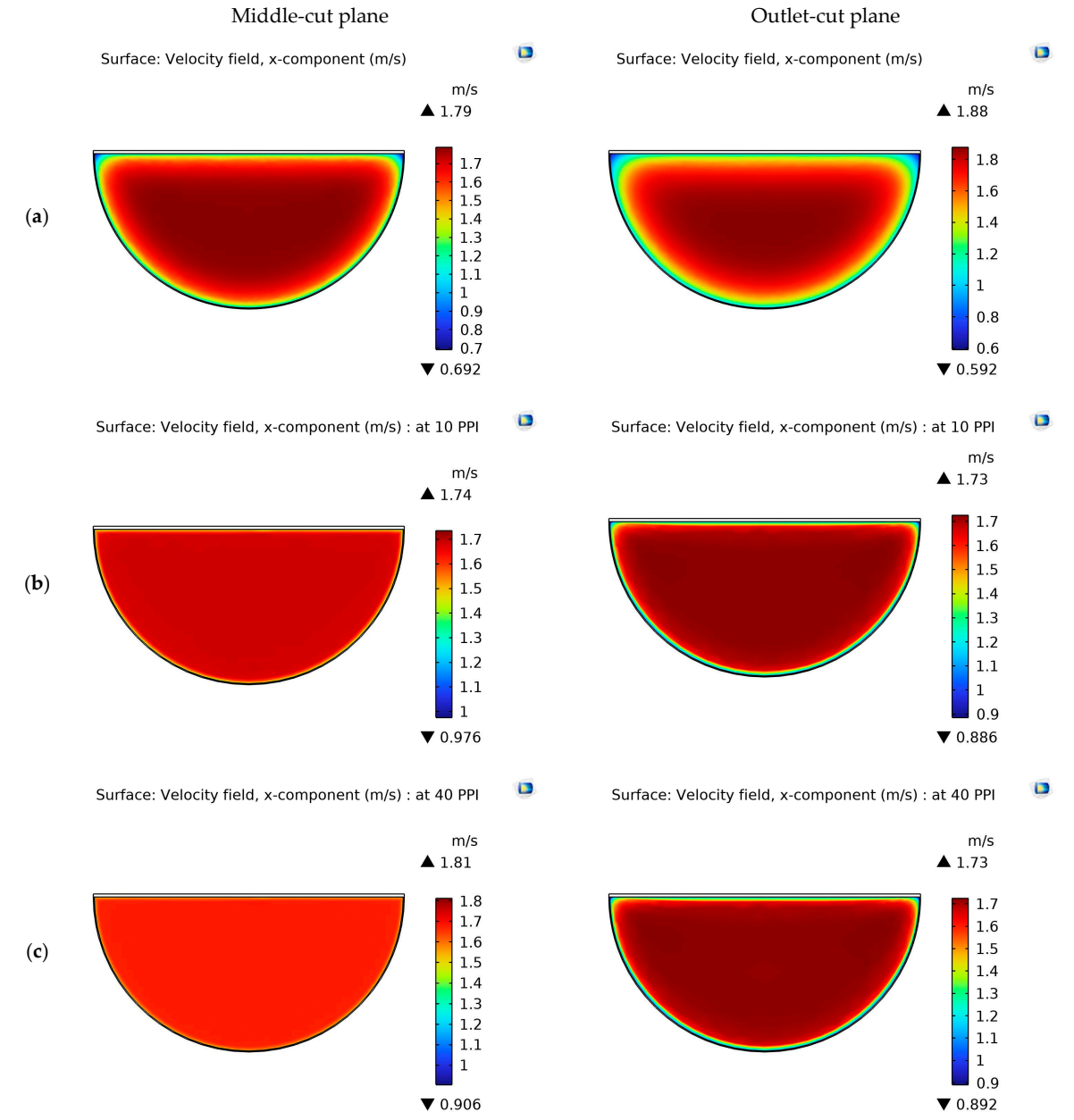

Figure 5. *Cont.*

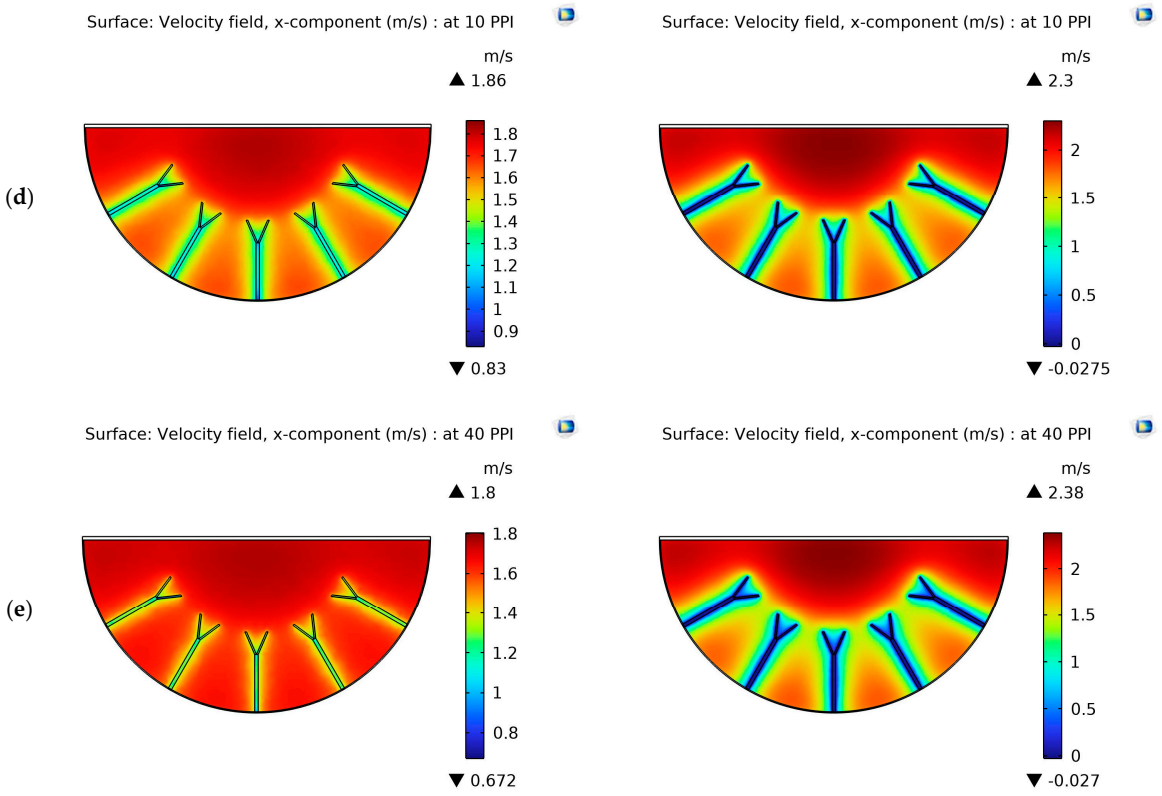

Figure 5. Velocity contours at $\dot{m}$ = 0.07 kg/s for (**a**) collector (I), (**b**) collector (II) 10 PPI, (**c**) collector (II) 40 PPI, (**d**) collector (III) 10 PPI, and (**e**) collector (III) 40 PPI.

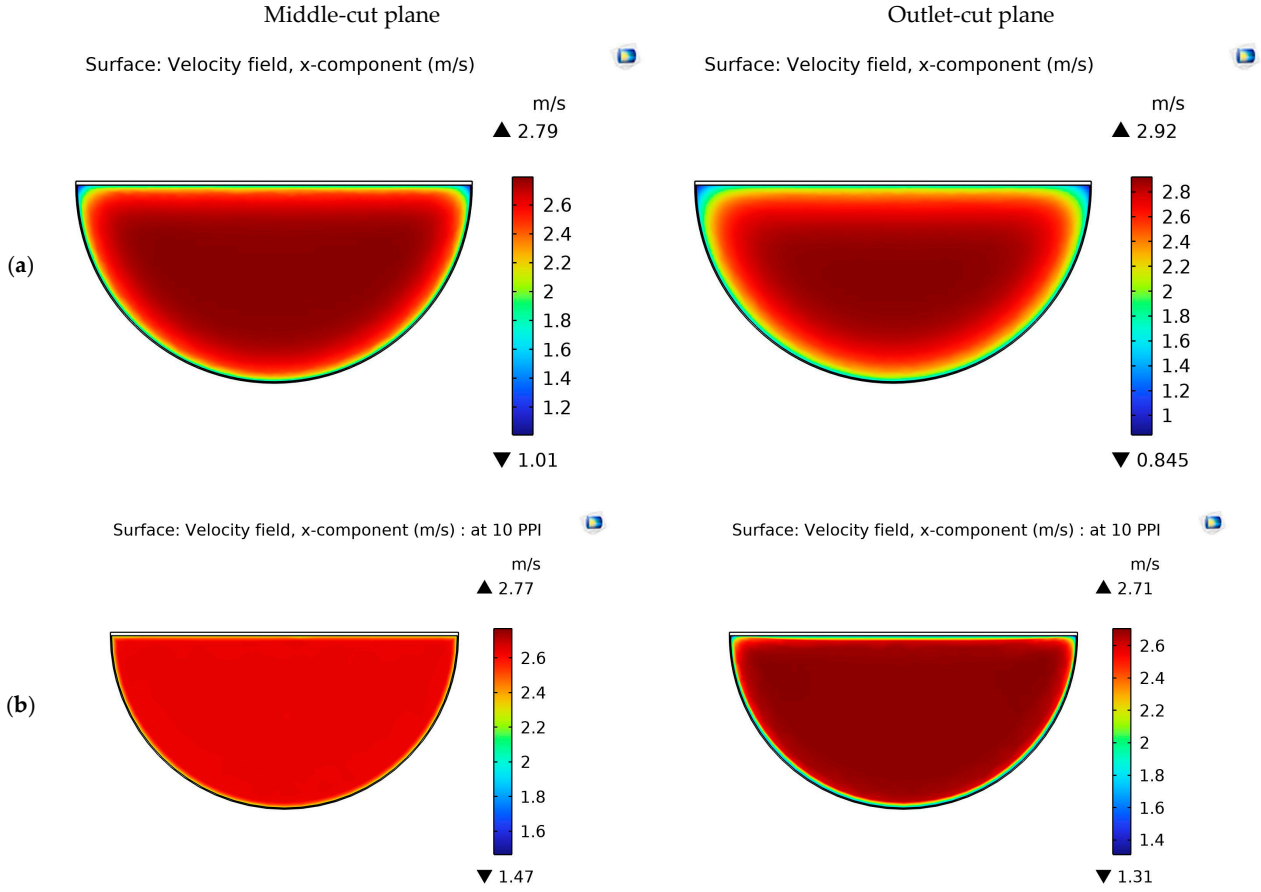

Figure 6. *Cont.*

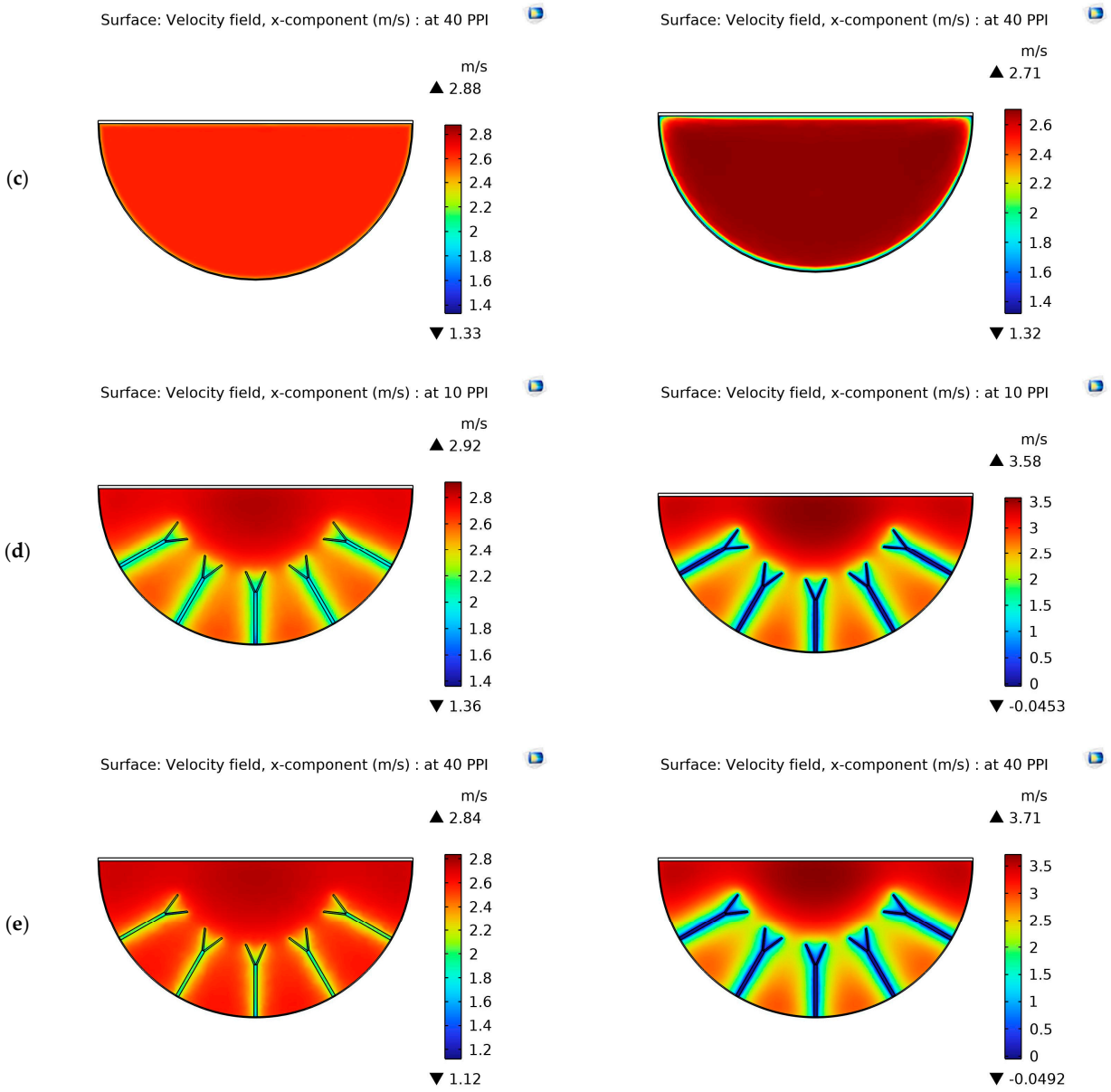

Figure 6. Velocity contours at $\dot{m} = 0.11$ kg/s for (**a**) collector (I), (**b**) collector (II) 10 PPI, (**c**) collector (II) 40 PPI, (**d**) collector (III) 10 PPI, and (**e**) collector (III) 40 PPI.

4.2. Pressure Contours

The pressure contours of the suggested designs for SCSAC with mass flow rates of only 0.03, 0.07, and 0.11 (kg/s) are presented in Figures 7–9. The pressure drop in the proposed models increases with mass flow rates. The effects of longitudinal porous Y-shaped fins are responsible for the larger pressure drops in model (III) compared to model (II). The pressure drops in SCSAC with metal foam samples of 40 PPI for models (II) and (III) are roughly twice those with 10 PPI samples. This is because the metal foam of the 40 PPI samples has more airflow resistance due to so many small-diameter pores, which can obstruct flow more significantly.

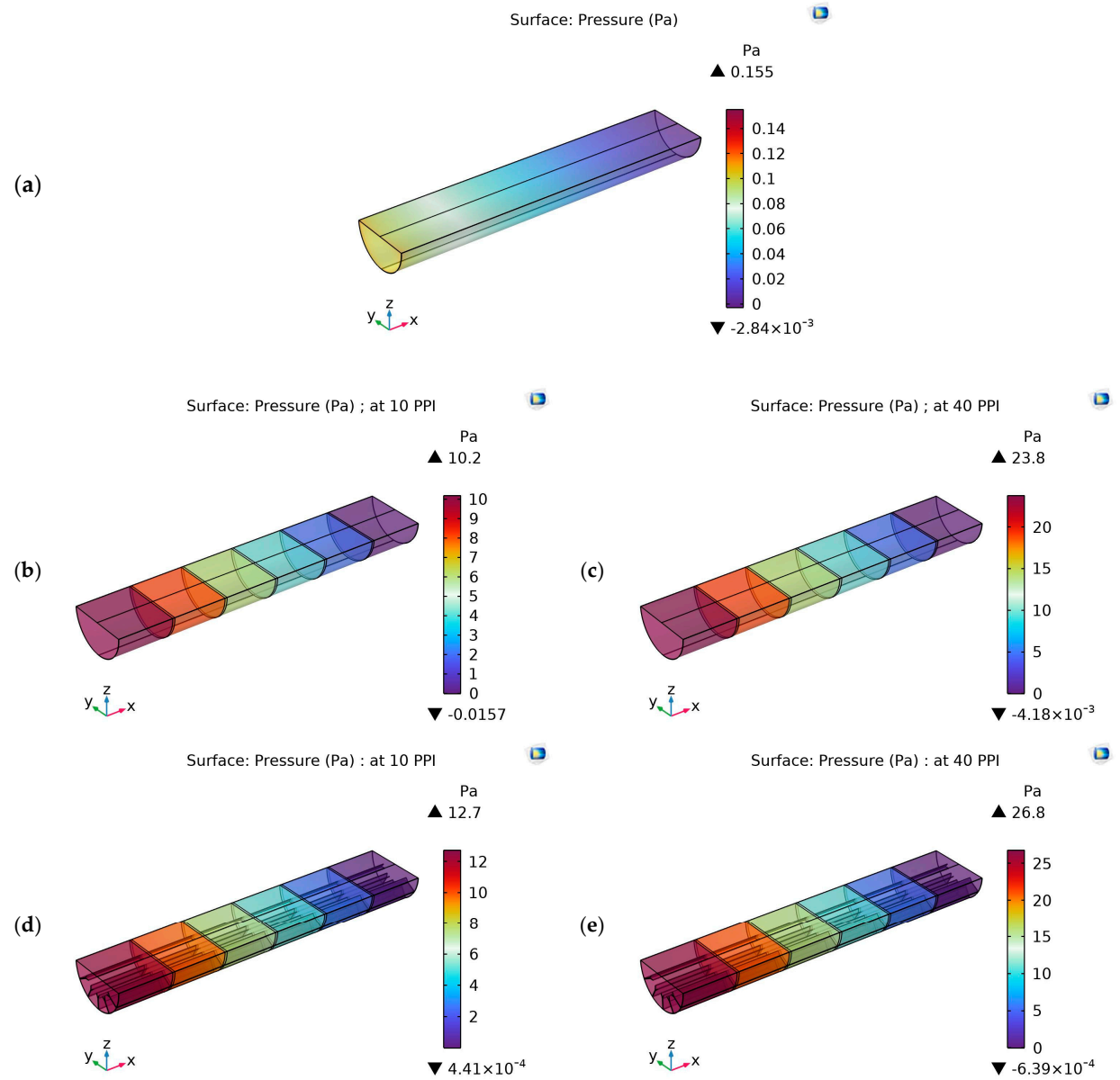

Figure 7. Pressure contours at $\dot{m} = 0.03$ kg/s for (**a**) collector (I), (**b**) collector (II) 10 PPI, (**c**) collector (II) 40 PPI, (**d**) collector (III) 10 PPI, and (**e**) collector (III) 40 PPI.

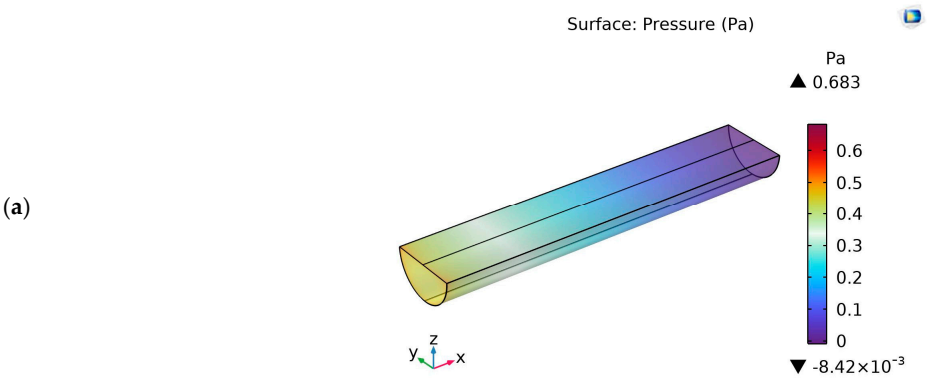

Figure 8. *Cont*.

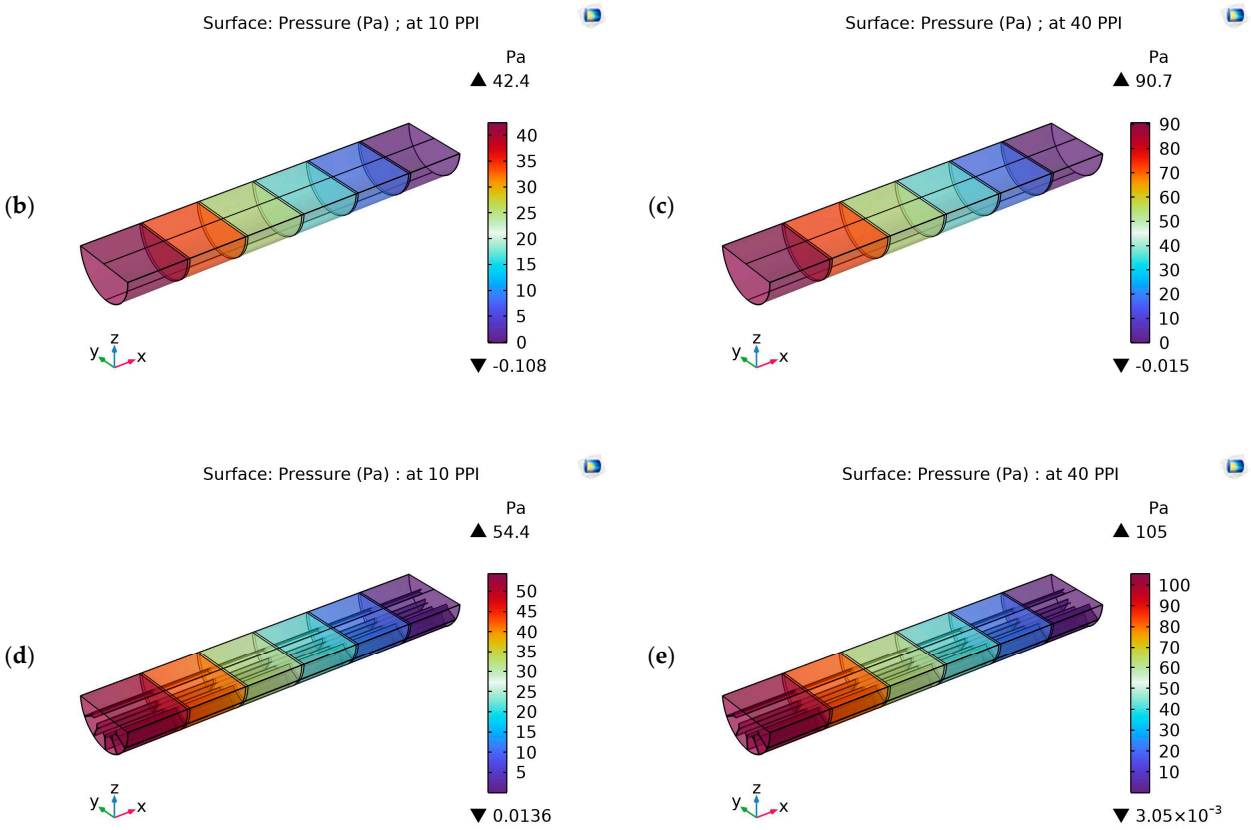

Figure 8. Pressure contours at $\dot{m} = 0.07$ kg/s for (**a**) collector (I), (**b**) collector (II) 10 PPI, (**c**) collector (II) 40 PPI, (**d**) collector (III) 10 PPI, and (**e**) collector (III) 40 PPI.

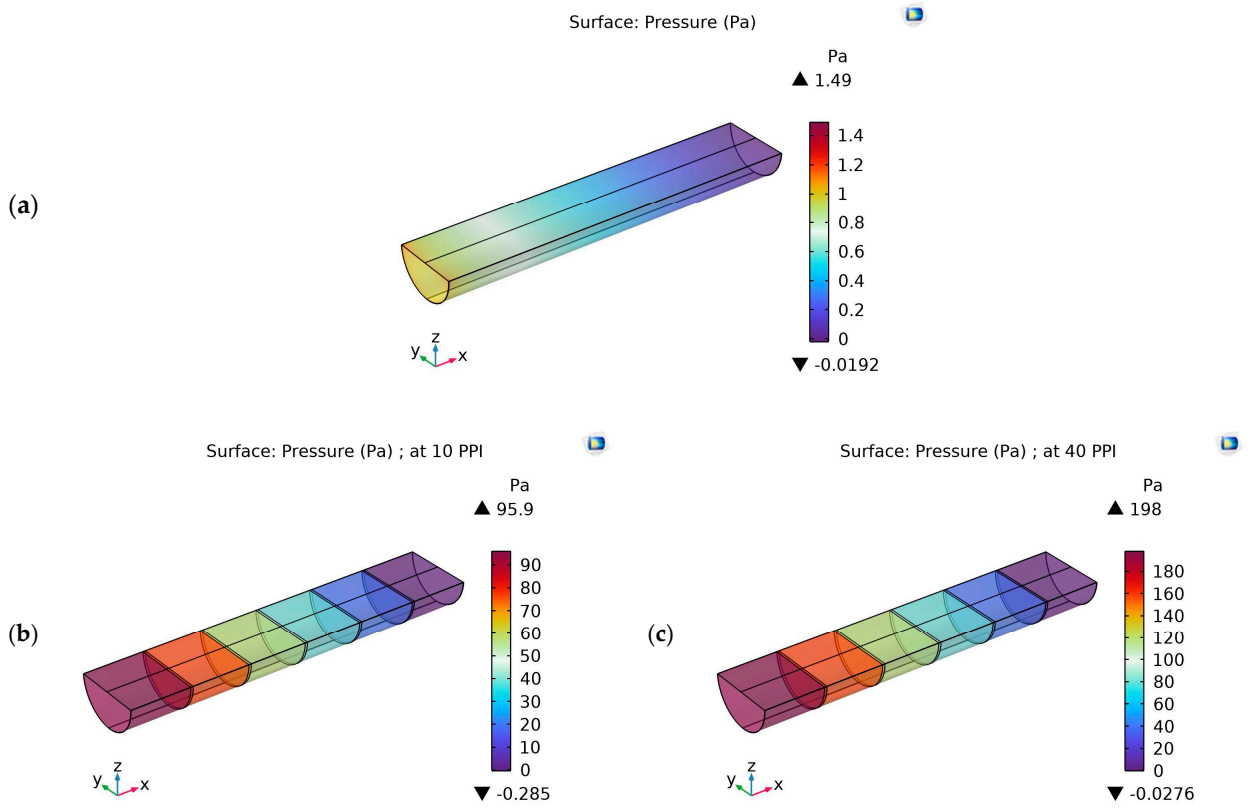

Figure 9. *Cont.*

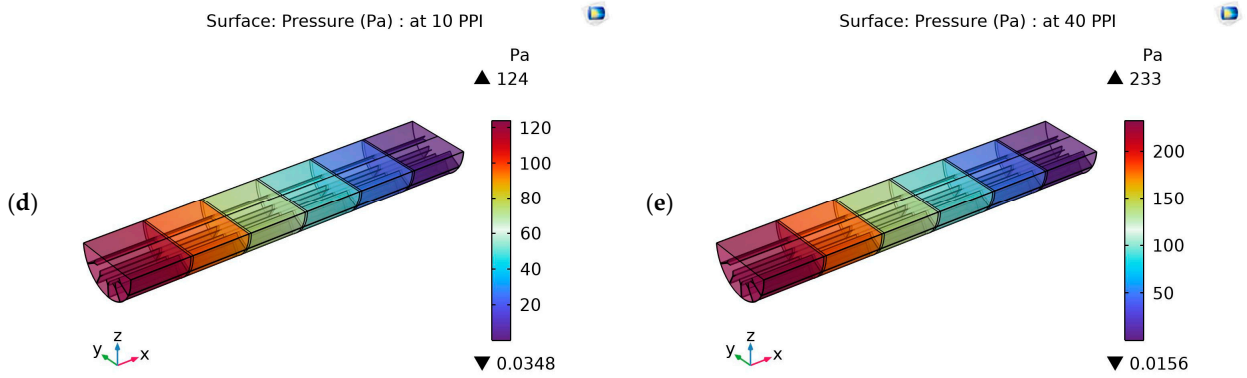

Figure 9. Pressure contours at $\dot{m} = 0.11$ kg/s for (**a**) collector (I), (**b**) collector (II) 10 PPI, (**c**) collector (II) 40 PPI, (**d**) collector (III) 10 PPI, and (**e**) collector (III) 40 PPI.

4.3. Temperature Contours

Figures 10–12 display the temperature contours of the proposed designs for SCSAC with mass flow rates of only 0.03, 0.07, and 0.11 (kg/s). Thermal boundary layer thickness decreases with increasing mass flow rate. Along the collector length of model (I), the thickness of the thermal boundary layer increases for adopted mass flow rates. The findings indicated that the air layers near the semicircular absorber plate had higher temperatures than those inside the collector's core. The metal foams prevent the thermal boundary layer from developing. According to the findings, the thermal boundary layer grew from the starting of the channel to the first semicircular metal foam, and between metal foams distributed along the length of the solar collector. In model (III), the configuration of the metal foams breaks down thermal boundary layers transversely and longitudinally. The findings demonstrated that the air layers along the interface surfaces between longitudinal metal foams and the air layers are hotter than the air layers in the center of the air channel.

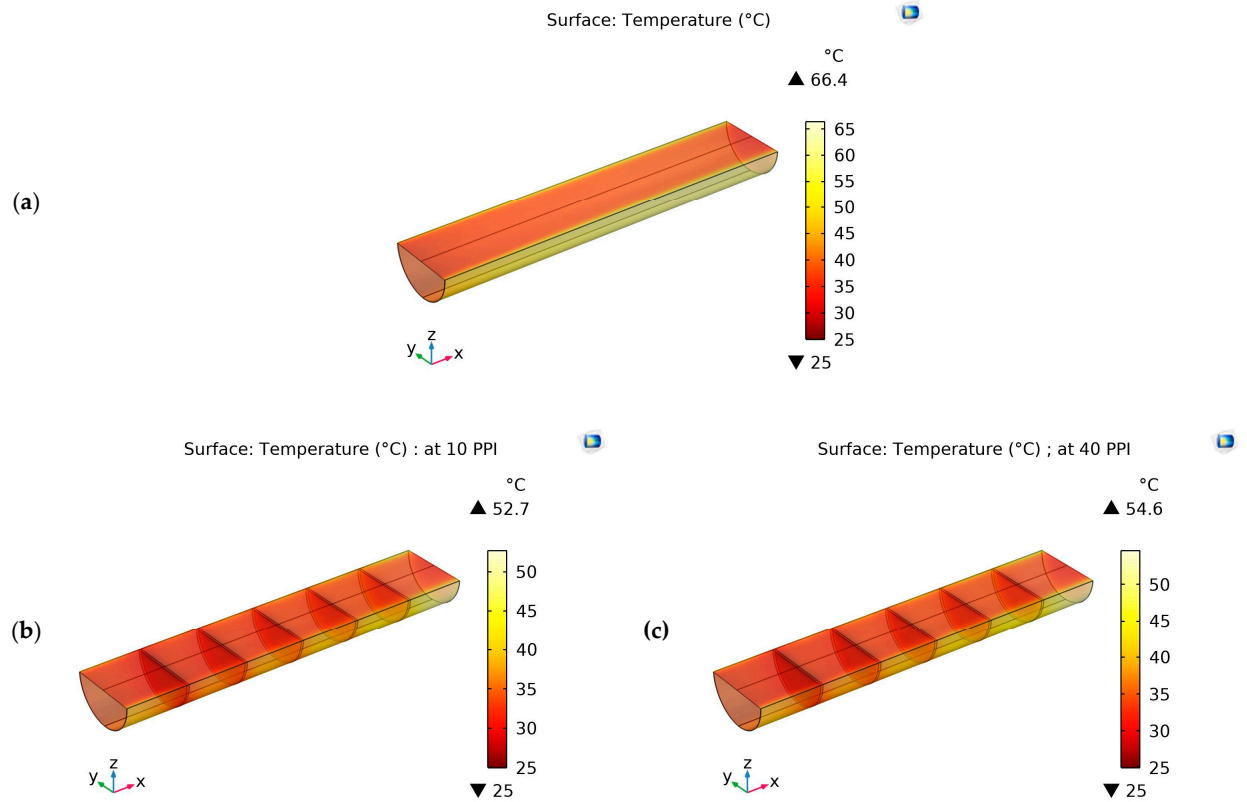

Figure 10. *Cont.*

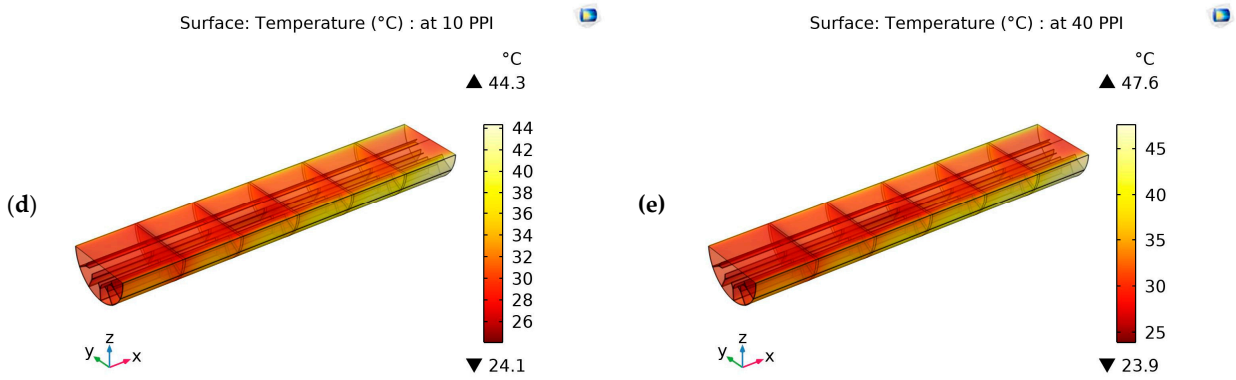

Figure 10. Temperature contours at $\dot{m}$ = 0.03 kg/s for (**a**) collector (I), (**b**) collector (II) 10 PPI, (**c**) collector (II) 40 PPI, (**d**) collector (III) 10 PPI, and (**e**) collector (III) 40 PPI.

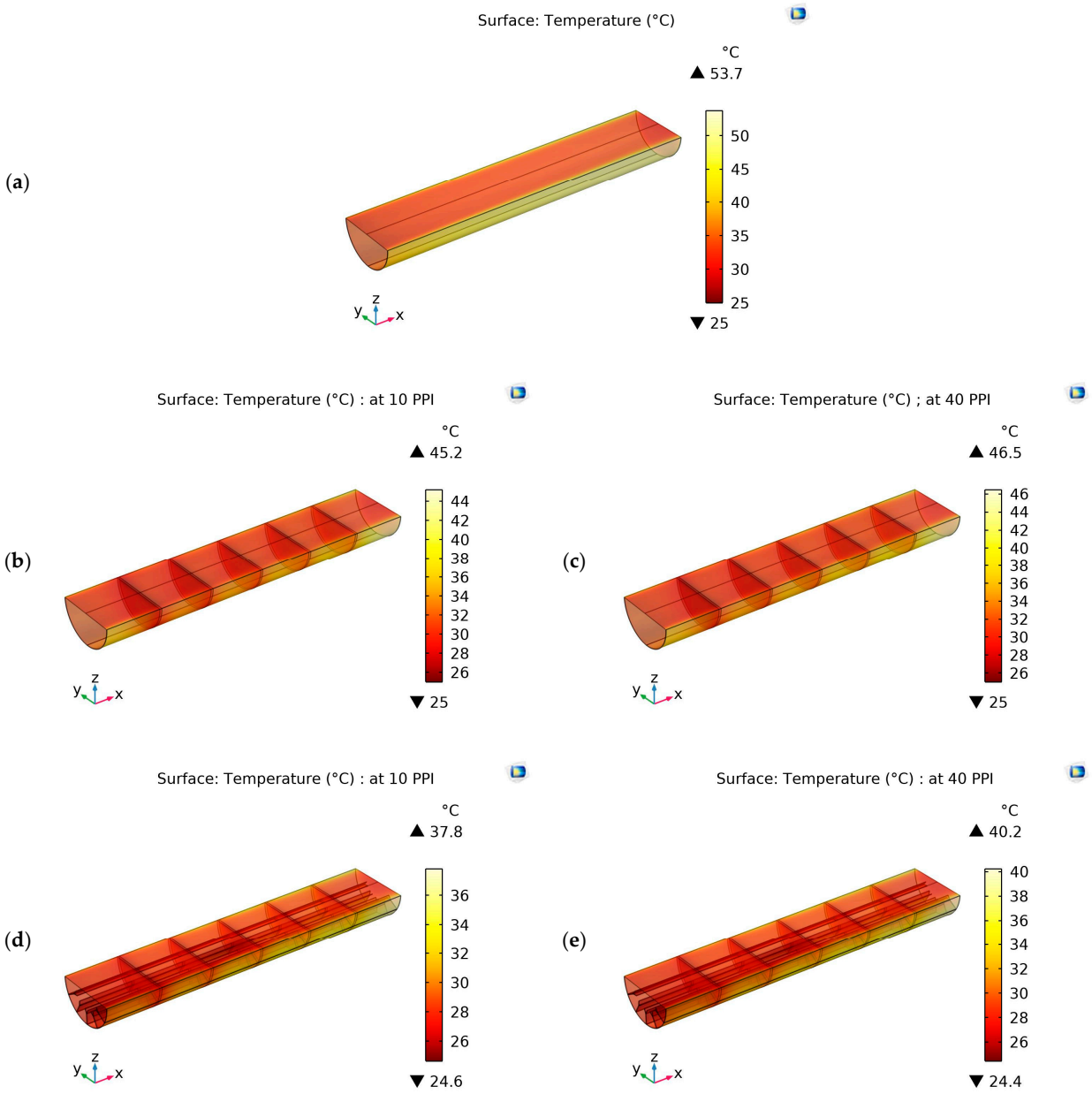

Figure 11. Temperature contours at $\dot{m}$ = 0.07 kg/s for (**a**) collector (I), (**b**) collector (II) 10 PPI, (**c**) collector (II) 40 PPI, (**d**) collector (III) 10 PPI, and (**e**) collector (III) 40 PPI.

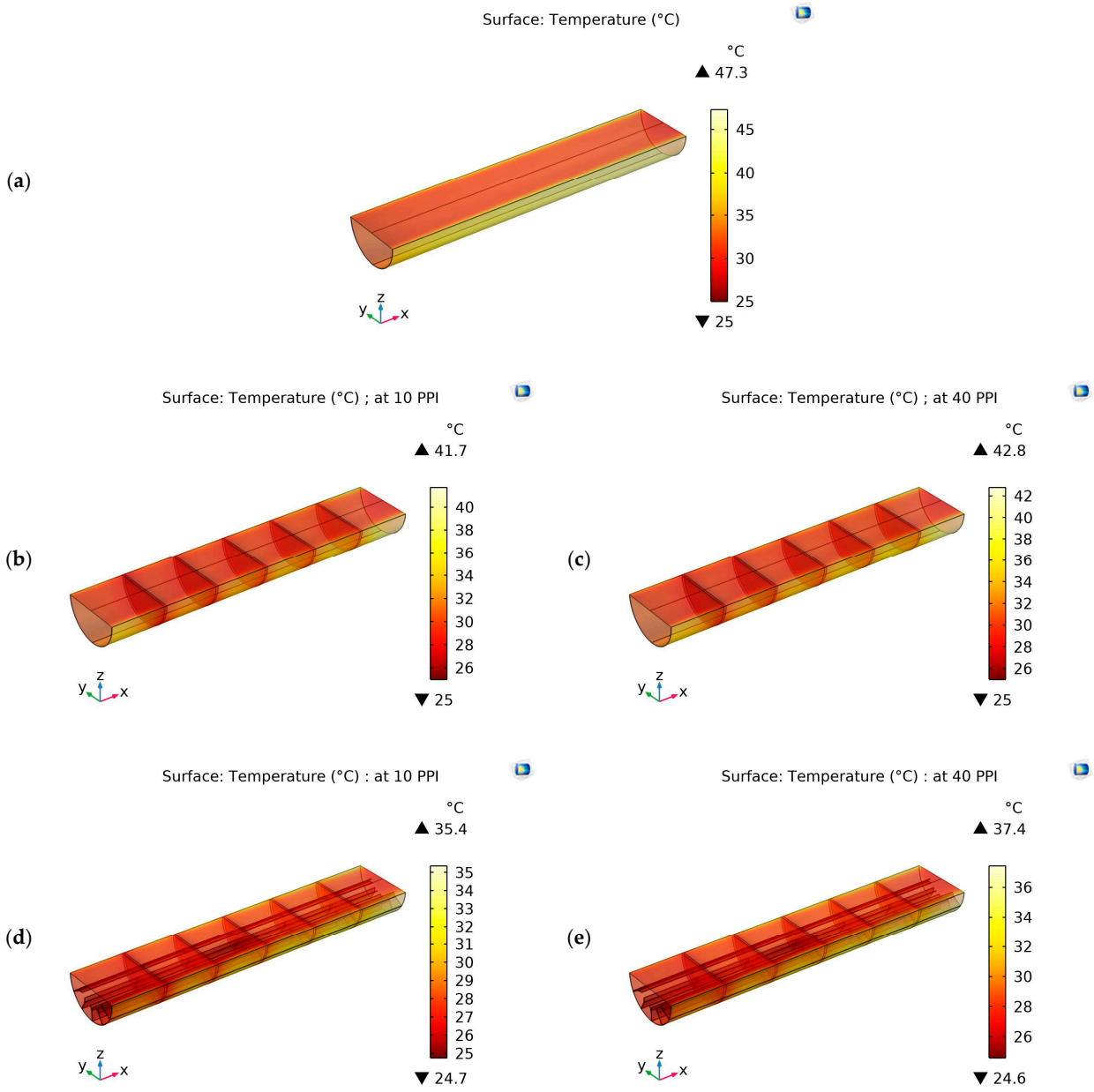

Figure 12. Temperature contours at $\dot{m} = 0.11$ kg/s for (**a**) collector (I), (**b**) collector (II) 10 PPI, (**c**) collector (II) 40 PPI, (**d**) collector (III) 10 PPI, and (**e**) collector (III) 40 PPI.

4.4. Outlet Air Temperature

Figure 13 shows the effect of the various mass fluxes on the temperature of the outlet air flow for all studied models. The outlet air temperature is determined by averaging the temperatures across the entire cross-sectional area at the exit of the air passage duct. In general, model (III) displays higher effort in extracting temperature from the collector than the other models at all mass flux values. However, model (II) shows a similar effect to model (III) with a slight gap between them; also, there is no clear effect of the PPI in either model. This may be attributed to the small difference in the porosity and the difference in the permeability between the two studied PPI samples. The outlet air temperatures from whole models decrease dramatically when mass fluxes increase. This could occur due to the excessive energy available when mass flux is low, which causes a high outlet air temperature. In simpler terms, the outlet air temperature decreases as mass flux increases due to the accelerated thermal exchange between the internal collector surfaces and the passing-through air. This rapid heat transfer leads to a decrease in the air temperature as it

exits the collector. In general, the outlet air temperature of all models is approximated to the same lowest value of 27 (°C) at 3.1124 (kg/m^2 s).

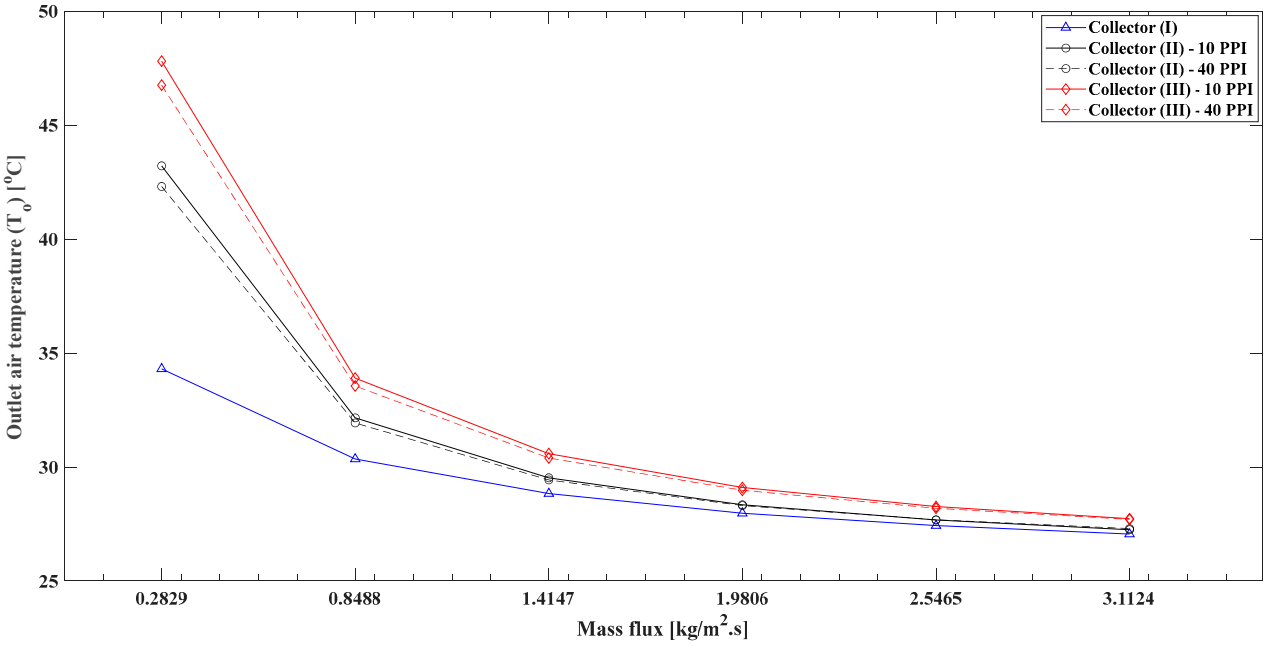

Figure 13. Outlet air temperature with the mass flux of proposed models.

Moreover, the outlet air temperature rise of models (II) and (III) compared to model (I) is statistically shown in Figure 14. It seems that there is an insignificant enhancement of the outlet air temperature rise obtained from model (II) with both PPI values; however, 10 PPI shows the highest enhancement with a small proportion. Model (III) displays a noticeable enhancement of the outlet air temperature rise with both PPI values. The effect of PPI was demolished for both models with an increase in mass flux. The highest increase in the outlet air temperature rise is approximately 13.5 °C at the lowest mass flux of 0.2829 kg/m^2 s, whereas the lowest enhancement is about 0.67 °C at the highest mass flux of 3.1134 kg/m^2 s for model (III) 10 PPI.

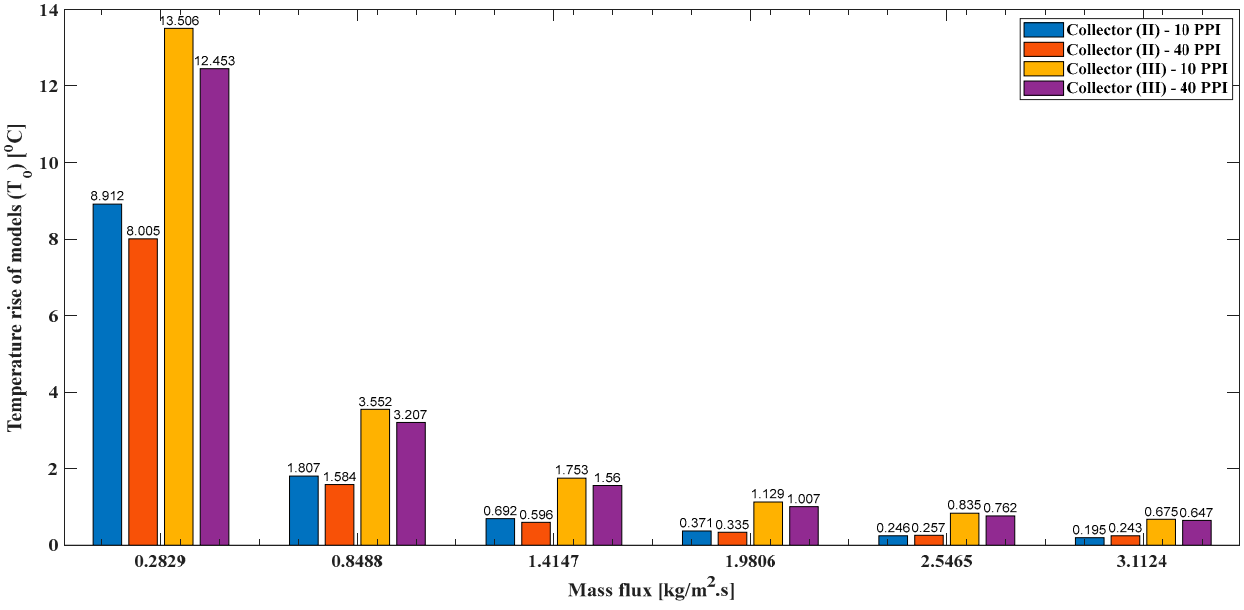

Figure 14. Air temperature rise of model (II) and model (III) in reference to model (I) versus mass flux.

4.5. Pressure Drops

Figure 15 declares the relation between the drop in pressure and the increase in the mass flux for all studied models. The two high-PPI models display more resistance to the increase in the mass flux, with model (III) being higher. The trends of the pressure drop curves start approximately from the same lower value and begin to increase and distinguished with the increase in mass flux. In other words, the effect of any filling in the air passage is demolished with low mass flux.

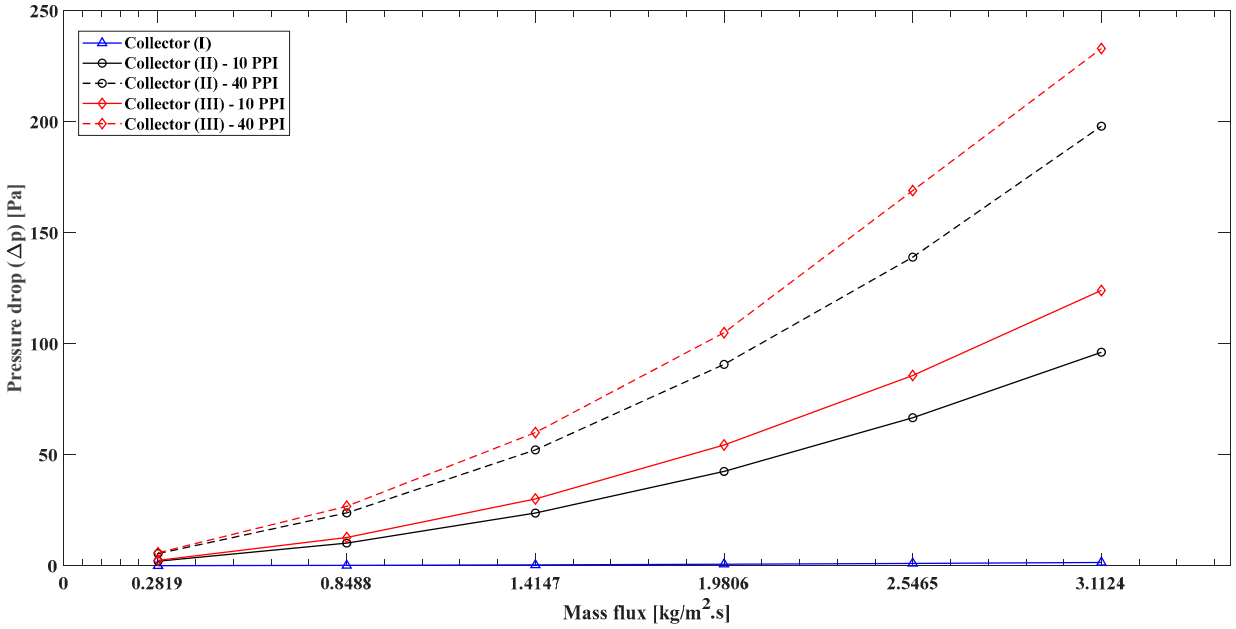

Figure 15. Pressure drops with the mass flux of proposed models.

The additional pressure drops of models (II) and (III) compared to model (I) can be represented statistically, as seen in Figure 16. The additional pressure drop of 40 PPI models is high when the mass flux is raised. The additional drop in pressure is 226.8 Pa for model (III) 40 PPI for 3.1124 kg/m^2 s, whereas it is just 5.7 Pa at 0.2819 kg/m^2 s.

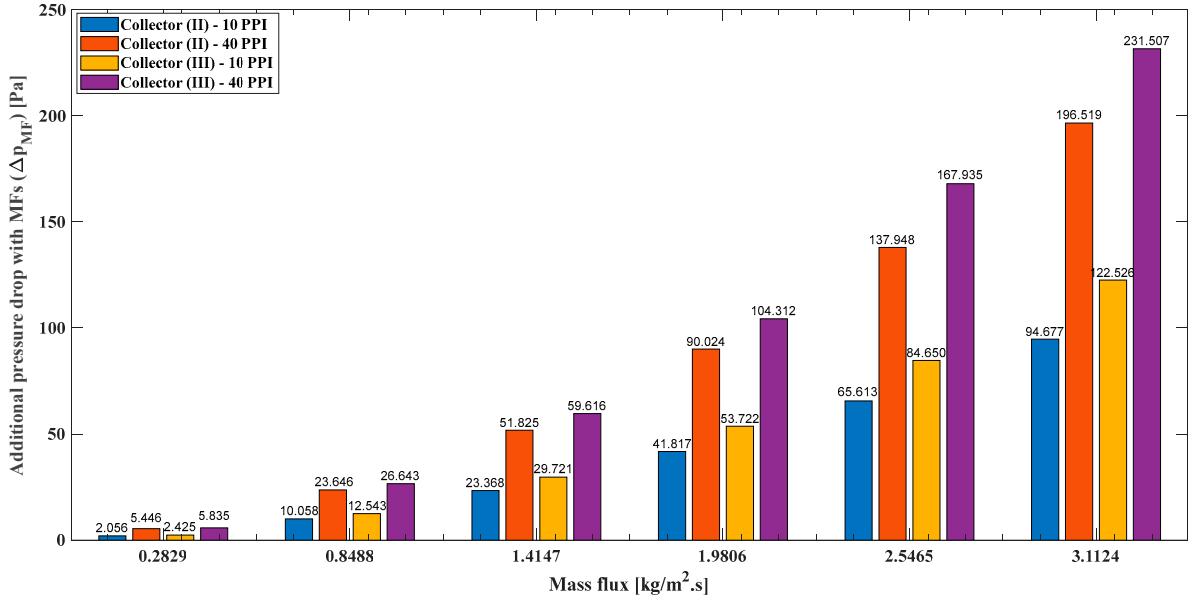

Figure 16. Additional pressure drop of models (II) and (III) in reference to model (I) versus mass flux.

4.6. Fan Power Consumption

Because of the high values of the pressure drop in the 40 PPI models, the run of the external fan requires a high power of 100–120 (W) when the mass flux raises to 3.11 (kg/m^2 s), as shown in Figure 17. The results of the additional fan power consumption can be signified statistically by models (II) and (III) compared to model (I), as shown in Figure 18. The fan consumes low added power in the 10 PPI models compared to the 40 PPI models and the clear air passage model. The additional fan power consumption rate increases more than double when the mass flux increases for each model.

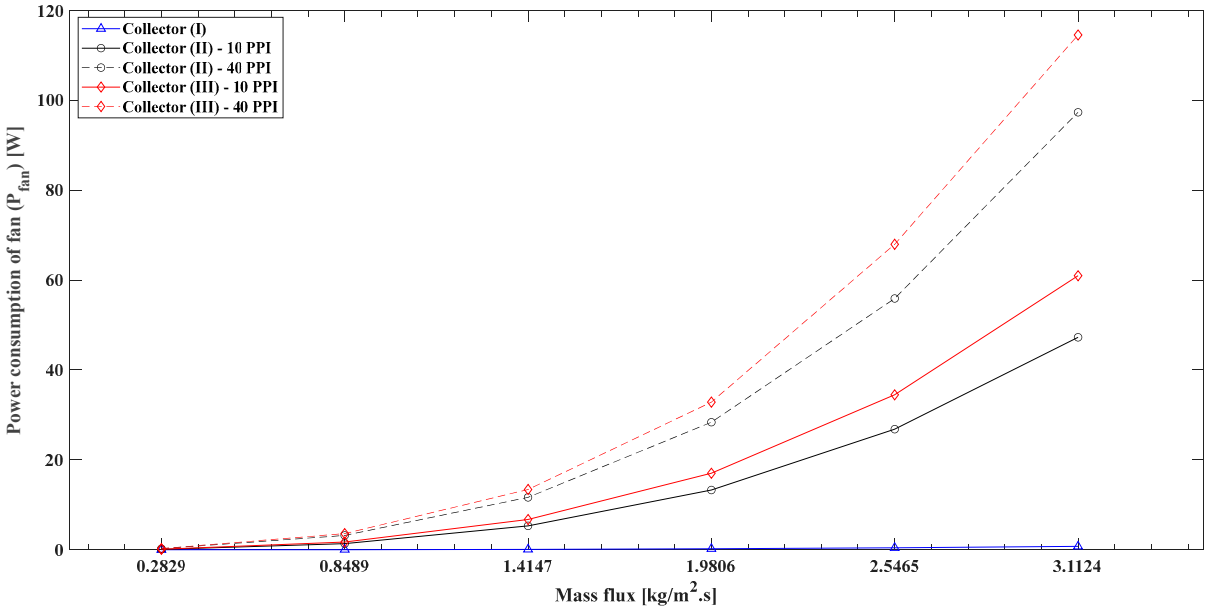

Figure 17. Fan power consumption with the mass flux of proposed models.

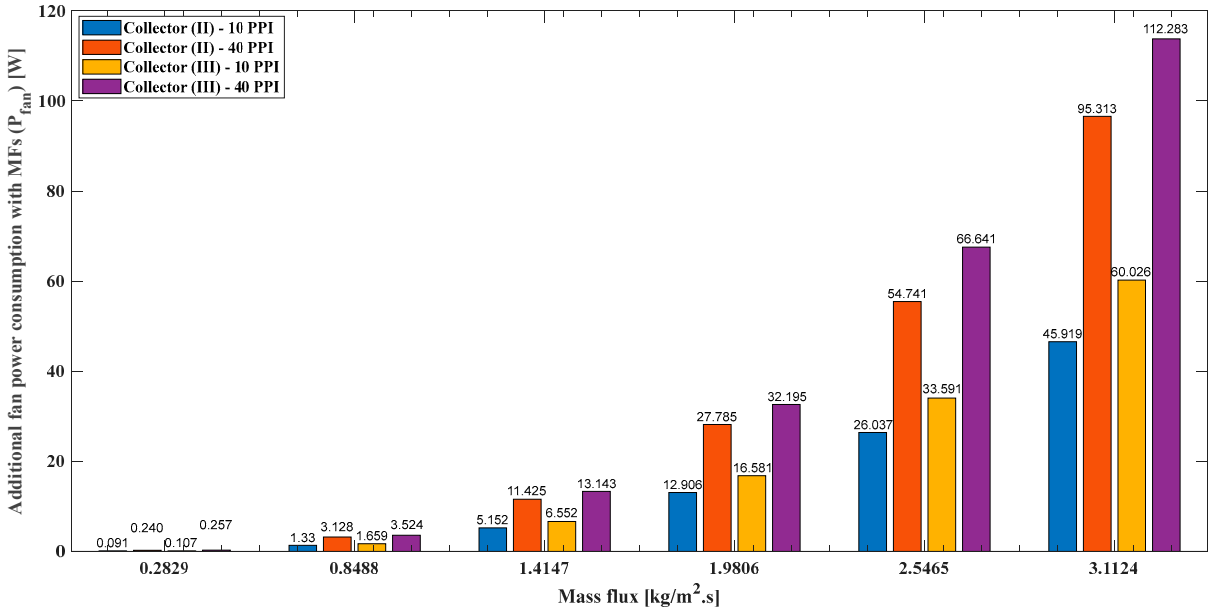

Figure 18. Additional fan power consumption of model (II) and model (III) in reference to model (I) versus mass flux.

4.7. Useful Heat Gain

The useful heat gain in a solar air collector refers to the net amount of thermal energy transferred to the air as it flows through the collector, resulting from the absorption of solar

radiation by the collector's absorber surface, minus any heat losses to the surroundings. The useful heat gain is noted to be highly consistent for all models. Nevertheless, the two types of model (III) contribute to an overall increase in the gain of useful heat up to 305 W. The configuration of model (III) could assist in containing more heat inside. The useful heat gain is always increasing with mass flux due to the high energy associated with increasing mass flux. There is also a slight difference between 10 PPI and 40 PPI, with 10 PPI being higher than 40 PPI for both models; this can be interpreted as the lower porosity of the 10 PPI compared to the 40 PPI, as seen in Figure 19.

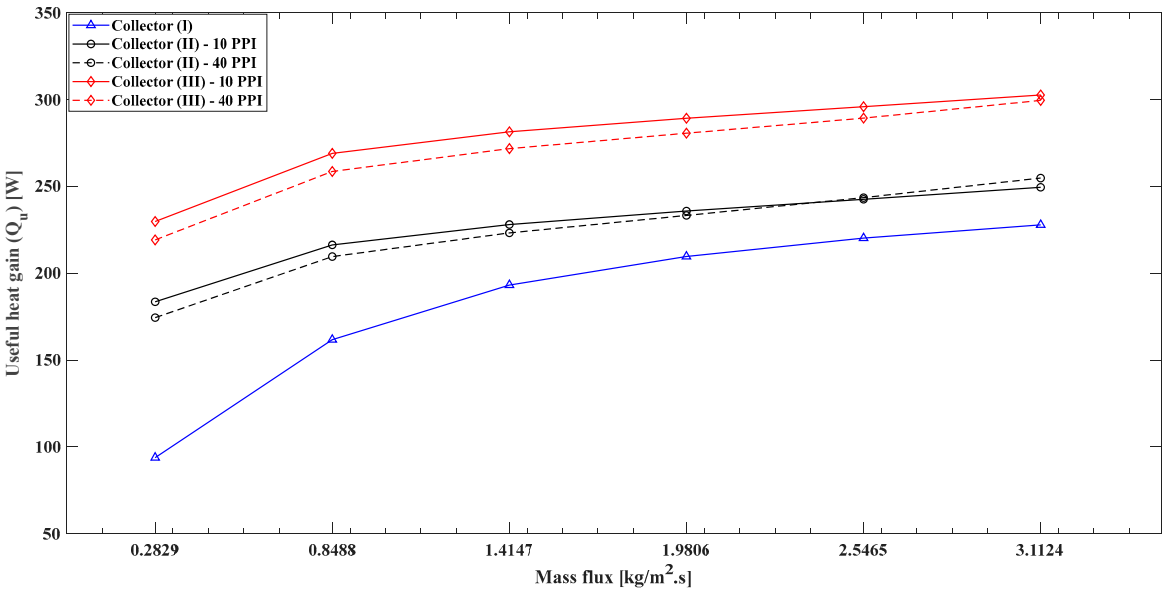

Figure 19. Useful heat gain with the mass flux of proposed models.

Additionally, Figure 20 declares statistical data for the rise in the useful heat gain of model (II) and model (III) compared to model (I). Model (III), 40 PPI, and 10 PPI could gain a heat rise up to 125 and 136 W, respectively, at the lowest mass flux, whereas the lowest heat gain rise is about 74 and 72 W, respectively, at the highest mass flux. Model (II) exhibits a lower heat gain rise than that of model (III) compared to model (I) for all mass fluxes.

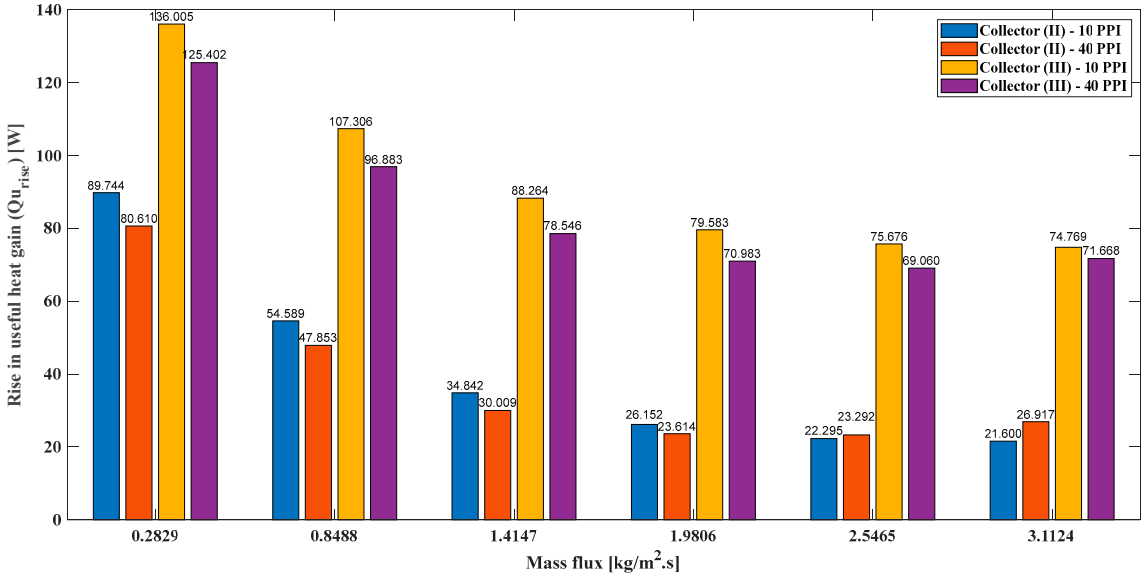

Figure 20. Rise in useful heat gain of model (II) and model (III) in reference to model (I) versus mass flux.

4.8. Thermal Efficiency

The thermal efficiency for all examined models is studied with various mass fluxes, as seen in Figure 21. The thermal efficiency increases with mass flux for all models. The results also reveal that model (III) performs about 25% and 35% better than model (II) and model (I), respectively. Moreover, the thermal efficiency of the collector configurations with metal foams of 10 PPI and 40 PPI is nearly identical, with a slight advantage for the 10 PPI foam. This difference is attributed to variations in porosity and permeability, as the 10 PPI foam has slightly lower porosity but three times higher permeability. As a result, both foams achieve similar thermal efficiency and outlet air temperatures. This indicates that a lower PPI value is sufficient for maintaining high thermal performance.

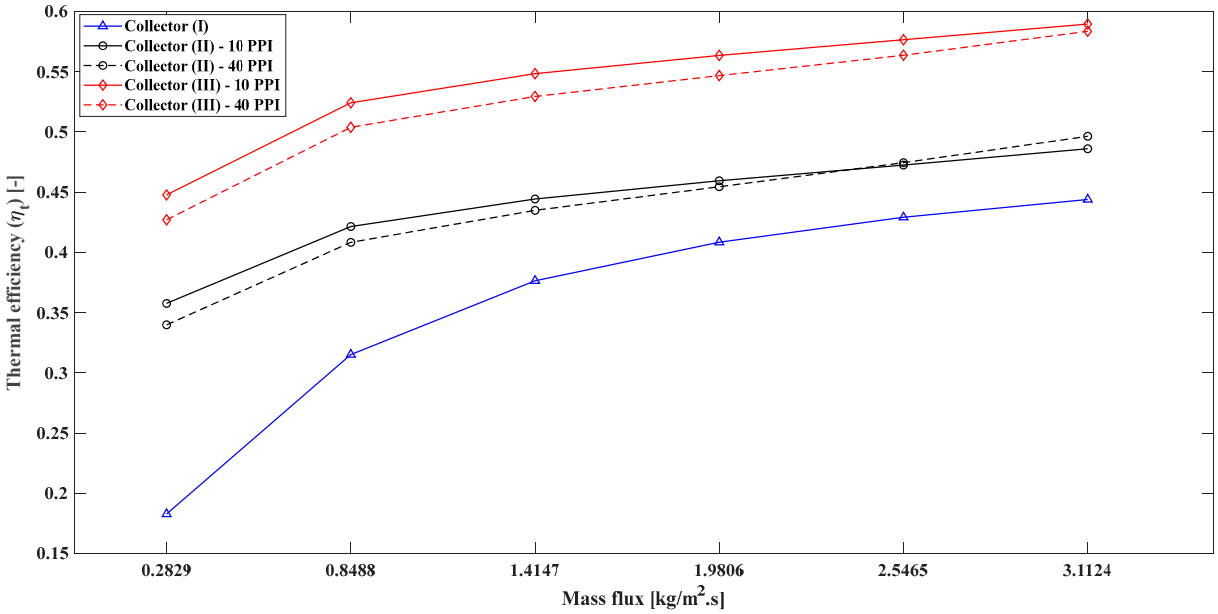

Figure 21. Thermal efficiency with mass flux of proposed models.

Furthermore, Figure 22 displays the percentage enhancement of the thermal efficiency of model (II) and model (III) compared to model (I) with various mass fluxes. Thermal efficiency percentage enhancement decreases with the increase in the mass flux. Model (III), 10 PPI, shows the highest percentage enhancement at various mass fluxes that can reach 145% at 0.2829 kg/m^2 s compared to model (I). Otherwise, model (II), 10 PPI, performs better than 40 PPI of the same model. However, at the highest value of mass flux, there is a noticeable equality between 10 PPI and 40 PPI of both models.

4.9. Thermo-Hydraulic Efficiency

Figure 23 depicts the thermo-hydraulic efficiency of the current models at various mass fluxes. Model (III) is still at the top compared to the other models. This could reveal the ability of this model to maintain heat corresponding to low flow resistance, which is enough to raise the thermo-hydraulic efficiency. Otherwise, model (I) exhibits enhancement when the mass fluxes increase with noticeable values and share the same thermo-hydraulic efficiency with other models at 2.5465 (kg/m^2 s), except for model (II), 40 PPI and model (III), 10 PPI. The general trend of the thermo-hydraulic efficiency increases with mass flux to a certain value for model (II) and model (III) at 1.4147 (kg/m^2 s) and then starts to decrease. However, model (I) keeps increasing with mass flux.

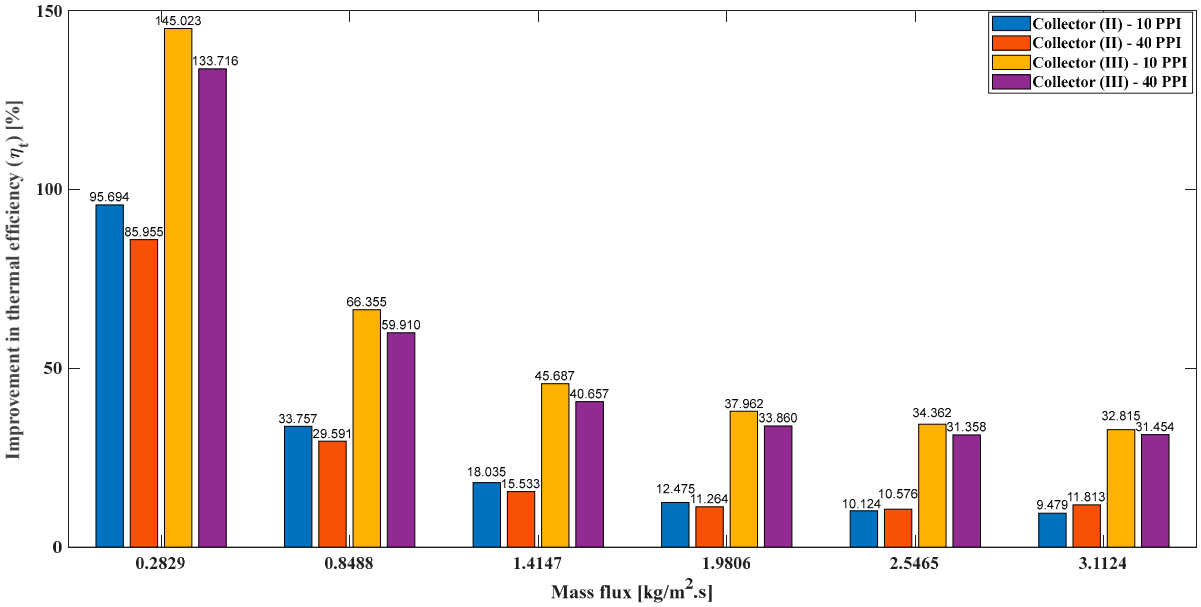

Figure 22. Percentage enhancement in thermal efficiency of model (II) and model (III) in reference to model (I) versus mass flux.

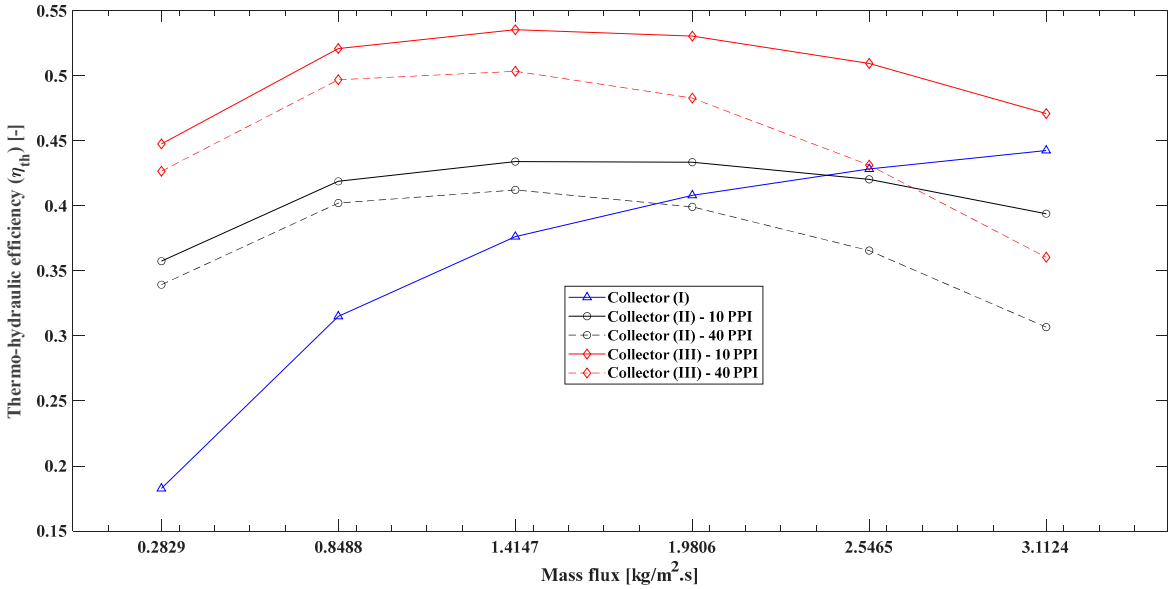

Figure 23. Thermo-hydraulic efficiency with the mass flux of proposed models.

Model (II) and model (III) with the two different PPI values are compared to that from model (I) in terms of thermo-hydraulic efficiency, as seen in Figure 24. In general, the thermo-hydraulic efficiency of model (III) 10 PPI, is the best among the other models. It reaches 145% at 0.2829 (kg/m^2 s) and then declines dramatically to about 7% at 3.1124 (kg/m^2 s) compared to model (I). This result confirms that model (III) 10 PPI, could provide lower flow resistance associated with heat transfer better than other models. Moreover, the increase in mass flux has an inverse effect on thermo-hydraulic efficiency compared to model (I), particularly at mass flux greater than 2 (kg/m^2 s) for other models. This can be attributed to the increase in the airflow resistance associated with the configuration of these models.

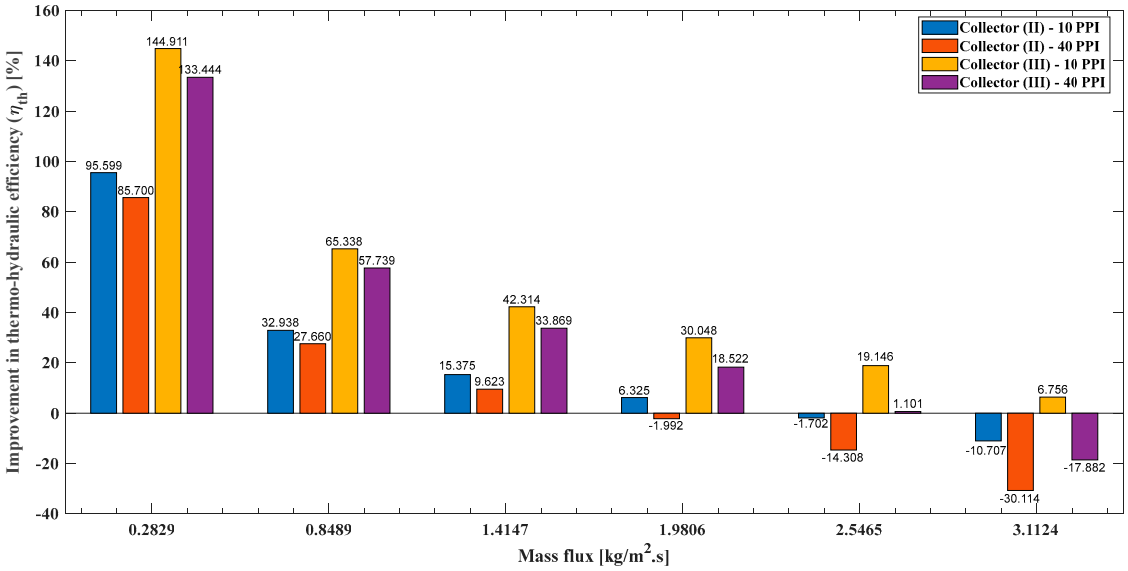

Figure 24. Percentage enhancement in thermo-hydraulic efficiency of models (II) and (III) in reference to model (I) versus mass flux.

4.10. Average Nusselt Number

Figure 25 refers to the obtained Nu from all studied models at various mass fluxes. The average Nu generally increases with the increase in the mass flux. Model (III), 10 PPI, produces the uppermost values of Nu_{av} compared to the other models. The dramatic increase in Nu_{av} could denote that the convection heat transfer of local Nu over the entire heat transfer surface is dominated over the effect of conduction. The existence of high PPI could provide adequate surface area to gain further convection heat transfer. Model (II) shows a minor effect in terms of PPI, while the PPI has a significant effect on model (III).

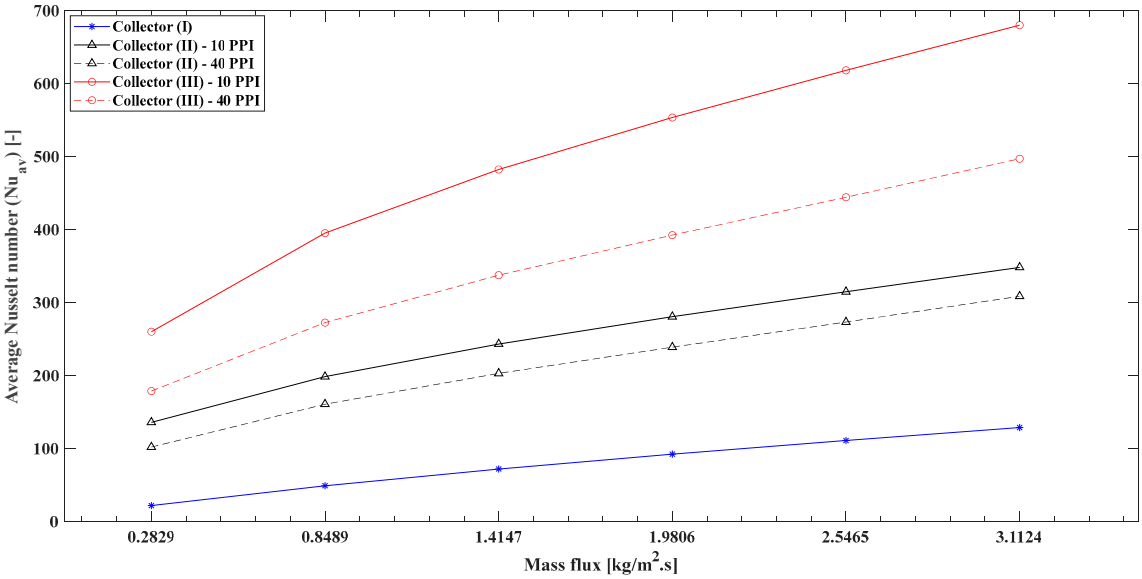

Figure 25. Average Nusselt number with mass flux.

4.11. Performance Evaluation Factor (PEF)

The performance evaluation factor (PEF) of the modified models against the mass flux is shown in Figure 26. Generally, all studied models show a decrease in the performance evaluation factor when the mass flux values increase. The PEF of the model (III) of 10 PPI is at the top of the categories. The PEF of this model exceeds the value of two at low mass flux.

However, this value declines to about one when the mass flux intensely rises. Model (III) 40 PPI, shows a similar manner to the previous model. Whereas results of model (II) declare a PEF below one in all cases except for 10 PPI, the PEF is higher than one when mass flux is between 0.3 and 0.85.

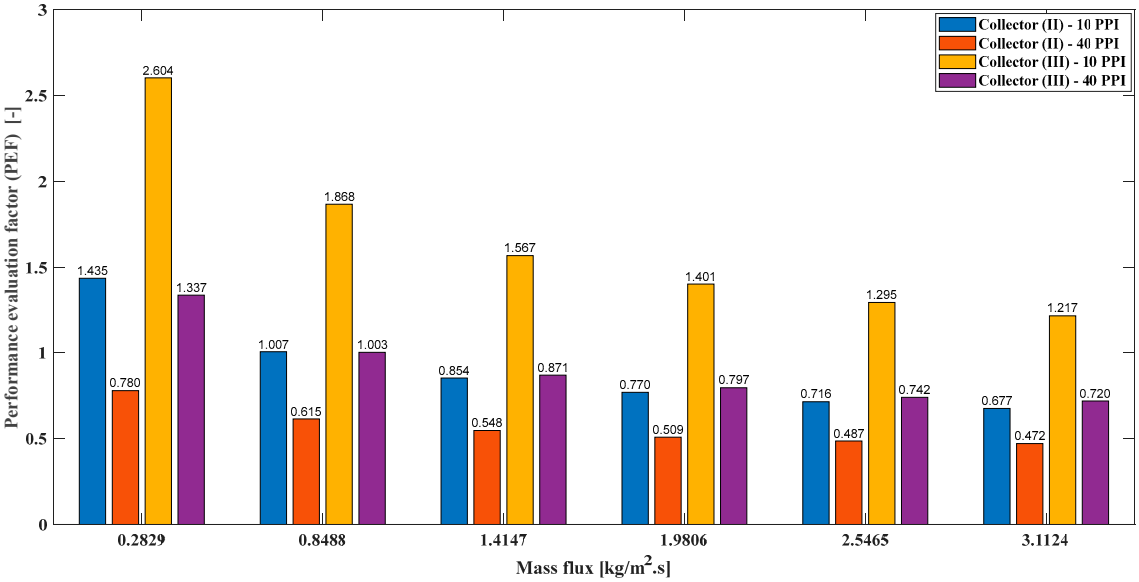

Figure 26. Performance evaluation factor (PEF) with mass flux of models (II) and (III).

5. Conclusions

The thermal and thermo-hydraulic performance of an SCSAC was simulated using COMSOL Multiphysics software version 6.2. The air passage was configured with three models: model (I) was with a clear semicircular air passage, while model (II) was with semicircular porous obstacles mounted in the passage of model (I), and model (III) was with Y-shaped porous fins and semicircular porous obstacles, also mounted in the passage of model (I). Aluminum metal foam of 10 PPI and 40 PPI was utilized for models (II) and (III).

The results revealed that the outlet air temperature decreased when the mass flux increased. The pressure drops increased with mass flux increases and with 40 PPI. The Nusselt number as well as the thermal and thermo-hydraulic efficiencies increased with mass flux. However, the thermo-hydraulic efficiency approached a high certain value and then decreased with mass flux. Model (III) 10 PPI, showed the highest performance of all proposed models, where the average outlet air temperature rise was about 7%; likewise, the thermal efficiency was about 30% higher. The PEF of model (III) 10 PPI, was always greater than one. It can be declared that equivalent thermal performance between metal foams with 10 PPI and 40 PPI can be achieved by making slight adjustments to properties such as porosity and permeability. This approach allows for either an exact or a closely similar thermal performance. It was evident that the thermal performance improved significantly with only 5% of the air passage volume occupied by metal foam.

Author Contributions: Conceptualization, B.A.R.A.-B. and A.M.R.; methodology, B.A.R.A.-B. and A.M.R.; software, B.A.R.A.-B. and A.M.R.; validation, B.A.R.A.-B. and A.M.R.; formal analysis, B.A.R.A.-B. and A.M.R.; investigation, B.A.R.A.-B., A.M.R. and A.O.A.-S.; resources, B.A.R.A.-B., A.M.R. and A.O.A.-S.; data duration, B.A.R.A.-B., A.M.R. and A.O.A.-S.; writing—original draft preparation, B.A.R.A.-B., A.M.R. and A.O.A.-S.; writing—review and editing, B.A.R.A.-B., A.M.R. and A.O.A.-S.; visualization, B.A.R.A.-B., A.M.R. and A.O.A.-S.; supervision, B.A.R.A.-B., A.M.R. and A.O.A.-S.; project administration, B.A.R.A.-B., A.M.R. and A.O.A.-S.; funding acquisition, B.A.R.A.-B., A.M.R. and A.O.A.-S. All authors have read and agreed to the published version of the manuscript.

Funding: This research received no external funding.

Data Availability Statement: Data are contained within the article.

Acknowledgments: The authors would like to express their appreciation and gratitude for the support they received from the University of Baghdad.

Conflicts of Interest: The authors declare no conflicts of interest.

Nomenclatures

A_d	Area of air duct, (m^2)
A_{sc}	Area of SCSAC, (m^2)
A_{s-ab}	Surface area of absorber plate, (m^2)
$C_{\varepsilon 1}$	Model coefficient, =1.44, $(-)$
$C_{\varepsilon 2}$	Model coefficient, =1.92, $(-)$
C_μ	Model coefficient, =0.09, $(-)$
CF	Conversion factor, $= 0.189$, $(-)$
C_F	Forchheimer coefficient, $(-)$
Cp	Heat capacity of air, $(J/kg \cdot K)$
C_{stpm}	Sub-grid turbulence generation by PM
D_h	Hydraulic diameter, (m)
e_b	Blackbody hemispherical emissive power
H	Height of duct, (m)
H_{fin}	Height of metal foam fin, (m)
F_s	Shape factor, $= \langle 1 \mp \cos(\beta) \rangle / 2$, $(-)$
G	Irradiation components at a given point
h_{co}	Combined HTC, $(W/m^2 \cdot K)$
h_{fc}	Forced convection HTC, $(W/m^2 \cdot K)$
h_{nc}	Natural convection HTC, $(W/m^2 \cdot °C)$
I	Identity tensor, $(-)$
I_s	Solar intensity, (W/m^2)
K	Viscous stress tensor, (Pa)
k	Turbulent kinetic energy, (m^2/s^2)
L_c	Characteristic length of collector, (m)
L_{sc}	Length of SCSAC, (m)
M_f	Mass flux, $(kg/m^2 \cdot s)$
$\dot{m}$	Mass flow rate, (kg/s)
N	Normal vector
p	Pressure, (Pa)
P_{fl}	Pumping power, (W)
P_{fn}	Fan power consumption, (W)
Pr	Prandtl number, $= \mu_a C_{pa} / \lambda_a$, $(-)$
P_w	Wetted perimeter, (m)
$\mathcal{P}_\varepsilon$	Production of TDR
$\mathcal{P}_{\varepsilon,pm}$	Production of TDR of porous matrix
$\mathcal{P}_k$	Production of TKE, due to velocity shear
$\mathcal{P}_{k,pm}$	Production of TKE of porous matrix
$q_{r,net}$	Net radiative heat source, (W/m^2)
Q_g'''	Heat generation in absorber plate, (W/m^3)
Q_{MF}'''	Heat generation in metal foam, (W/m^3)
Ra	Rayleigh number $= \left(g\beta \Delta T L^3 / \alpha v \right)$, $(-)$
Re_L	Reynolds number, $= \rho_a V_w L / \mu_a$, $(-)$
T	Temperature, (°C)
T_{in}	Inlet temperature, (°C)
T_{init}	Initial temperature, (°C)
T_{amb}	Ambient air temperature, (°C)
T_g	Temperature of glass cover, (°C)
T_p	Temperature of absorber plate, (°C)
T_{sk}	Sky temperature, (°C)
t_{fin}	Thickness of metal foam fin, (m)
t_g	Thickness of glass cover, (m)
t_p	Thickness of absorber plate, (m)
$\vec{V}$	Velocity vector, (m/s)
V_{init}	Initial velocity, (m/s)
V_w	Wind velocity, (m/s)
W_{sc}	Width of SCSAC, (m)
$\langle \rangle^i$	Intrinsic average of parameter

Greek letters

α	Thermal diffusivity, (m^2/s)
α_g	Absorptivity of glass cover, $(-)$
α_p	Absorptivity of absorber plate, $(-)$
β	Tilt angle of solar collector, $(^\circ)$
ε	Turbulence dissipation rate TDR, (m^2/s^3)
ϵ_g	Emissivity of glass cover, $(-)$
ϵ_p	Emissivity of absorber plate, $(-)$
η_t	Thermal efficiency, $(-)$
η_{th}	Thermo-hydraulic efficiency, $(-)$
κ	Permeability of metal foam, (m^2)
λ_a	Air thermal conductivity, $(W/m \cdot °C)$
λ_f	Thermal conductivity of air in PM, $(W/m \cdot °C)$
λ_s	Thermal conductivity of PM, $(W/m \cdot °C)$
μ	Dynamic viscosity, $(Pa \cdot s)$
μ_T	Turbulent dynamic viscosity, $(Pa \cdot s)$
ν	Kinetic viscosity, (m^2/s)
ρ	Density of air inside the duct, (kg/m^3)
ρ_a	Density of air outside the SAC, (kg/m^3)
σ	Stefan Boltzmann constant, $\left(W/m \cdot K^4\right)$
σ_k	Stress tensor of TKE, =1.0, $(-)$
σ_ε	Stress tensor of TDR, =1.3, $(-)$
τ_g	Transmissivity of glass cover, $(-)$
$\varnothing_p$	Porosity of metal foam, $(-)$

Abbreviations

FEM	Finite element method
FR	Free region
HTC	Heat transfer coefficient
PR	Porous region
PARDISO	Parallel sparse direct solver
PPI	Pore per inch
SAC	Solar air collector
SCSAC	Semicircular solar air collector
TDR	Turbulent dissipation rate
TKE	Turbulent kinetic energy

References

1. Al-Bakri, B.A.R.; Rasham, A.M.; Al-Sulttani, A.O. Thermal Performance of Multiple-Pass Solar Air Heater with Pin Fins. *J. Eng. Sci. Technol.* **2022**, *17*, 2192–2217.
2. Peng, H.; Ling, X. Analysis of heat transfer and flow characteristics over serrated fins with different flow directions. *Energy Convers. Manag.* **2011**, *52*, 826–835. [CrossRef]
3. Priyam, A.; Chand, P. Experimental investigations on thermal performance of solar air heater with wavy fin absorbers. *Heat Mass Transf.* **2019**, *55*, 2651–2666. [CrossRef]
4. Singh, S.; Dhruw, L.; Chander, S. Experimental investigation of a double pass converging finned wire mesh packed bed solar air heater. *J. Energy Storage* **2019**, *21*, 713–723. [CrossRef]
5. Gabhane, M.G.; Kanase-Patil, A.B. Experimental analysis of double flow solar air heater with multiple C shape roughness. *Sol. Energy* **2017**, *155*, 1411–1416. [CrossRef]
6. Kabeel, A.; Hamed, M.H.; Omara, Z.; Kandeal, A. Influence of fin height on the performance of a glazed and bladed entrance single-pass solar air heater. *Sol. Energy* **2018**, *162*, 410–419. [CrossRef]
7. Kumar, R.; Chand, P. Performance prediction of extended surface absorber solar air collector with twisted tape inserts. *Sol. Energy* **2018**, *169*, 40–48. [CrossRef]
8. Abdullah, A.S.; Abou Al-sood, M.M.; Omara, Z.M.; Bek, M.A.; Kabeel, A.E. Performance evaluation of a new counter flow double pass solar air heater with turbulators. *Sol. Energy* **2018**, *173*, 398–406. [CrossRef]
9. Priyam, A.; Chand, P. Effect of wavelength and amplitude on the performance of wavy finned absorber solar air heater. *Renew. Energy* **2018**, *119*, 690–702. [CrossRef]
10. Tarminzi, M.A.S.M.; Razak, A.A.; Azmi, M.A.A.; Fazlizan, A.; Majid, Z.A.A.; Sopian, K. Comparative study on thermal performance of cross-matrix absorber solar collector with series and parallel configurations. *Case Stud. Therm. Eng.* **2021**, *25*, 100935. [CrossRef]
11. Rasham, A.M.; Al-Bakri, B.A.R. *Thermal Performance of Double-Pass Counter Flow and Double-Parallel Flow Solar Air Heater with V-Grooved Absorber Plate*; IOP Publishing: Bristol, UK, 2021.
12. Farhan, A.A.; Sahi, H.A. Energy Analysis of Solar Collector With perforated Absorber Plate. *J. Eng.* **2017**, *23*, 89–102. [CrossRef]
13. Hussain, M.K.; Rasham, A.M.; Alshadeedi, B.M. *Finite Element Modeling of Finned Double-Pass Solar Air Heaters*; IEEE: Lahore, Pakistan, 2021.
14. Kabeel, A.; Khalil, A.; Shalaby, S.; Zayed, M. Experimental investigation of thermal performance of flat and v-corrugated plate solar air heaters with and without PCM as thermal energy storage. *Energy Convers. Manag.* **2016**, *113*, 264–272. [CrossRef]
15. Abuşka, M.; Şevik, S. Energy, exergy, economic and environmental (4E) analyses of flat-plate and V-groove solar air collectors based on aluminium and copper. *Sol. Energy* **2017**, *158*, 259–277. [CrossRef]
16. Chamoli, S.; Lu, R.; Xu, D.; Yu, P. Thermal performance improvement of a solar air heater fitted with winglet vortex generators. *Sol. Energy* **2018**, *159*, 966–983. [CrossRef]
17. Jassim, N.A.; Shbailat, S.J. Energy and Exergy Analysis of Dual Channel Solar Air Collector with Different Absorber Plates Geometry. *J. Eng.* **2018**, *24*, 19–40. [CrossRef]
18. Mustafa, M.T.; Mustafa, A.T. Numerical Simulation of Thermal-Hydrodynamic Behavior within Solar Air Collector. *J. Eng.* **2018**, *24*, 29–41. [CrossRef]
19. Mahdi, M.M.; Gaddoa, A.A. Outdoor Testing of a Zig-Zag SolarAir heater with and without Artificial Roughness on Absorber Plate. *J. Eng.* **2019**, *25*, 1–17.
20. Chen, C.-C.; Huang, P.-C. Numerical study of heat transfer enhancement for a novel flat-plate solar water collector using metal-foam blocks. *Int. J. Heat Mass Transf.* **2012**, *55*, 6734–6756. [CrossRef]
21. Nima, M.A.; Ali, A.M. Effect of Metal Foam Insertion on Thermal Performance of Flat-PlateWater Solar Collector Under Iraqi Climate Conditions. *Arab. J. Sci. Eng.* **2017**, *42*, 4863–4884. [CrossRef]
22. Nima, M.A.; Ali, A.M. Numerical Study of Heat Transfer Enhancement for a Flat Plate Solar Collector by Adding Metal Foam Blocks. *J. Eng.* **2017**, *23*, 13–32. [CrossRef]
23. Singh, S. Experimental and numerical investigations of a single and double pass porous serpentine wavy wiremesh packed bed solar air heater. *Renew. Energy* **2020**, *145*, 1361–1387. [CrossRef]
24. Taha, S.Y.; Farhan, A.A. Performance augmentation of a solar air heater using herringbone metal foam fins: An experimental work. *Int. J. Energy Res.* **2020**, *45*, 2321–2333. [CrossRef]
25. Jobair, H.K.; Nima, M.A. The indirect solar dryers with innovative solar air heaters designs: A review article. *Heat Transf.* **2023**, *52*, 2400–2436. [CrossRef]
26. Lakshmi, D.; Layek, A.; Kumar, P.M. Performance analysis of trapezoidal corrugated solar air heater with sensible heat storage material. *Energy Procedia* **2017**, *109*, 463–470. [CrossRef]
27. Zhou, X. Thermal performance of curved-slope solar collector. *Int. J. Heat Mass Transf.* **2020**, *150*, 119295. [CrossRef]

28. Zhao, Y.; Meng, T.; Jing, C.; Hu, J.; Qian, S. Experimental and numerical investigation on thermal performance of PV-driven aluminium honeycomb solar air collector. *Sol. Energy* **2020**, *204*, 294–306. [CrossRef]
29. Mahboub, C.; Moummi, N.; Brima, A.; Moummi, A. Experimental study of new solar air heater design. *Int. J. Green Energy* **2016**, *13*, 521–529. [CrossRef]
30. Pfister, H.; Ralston, T.; Kim, S.W. A novel gridded solar air heater and an investigation of its conversion efficiency. *Sol. Energy* **2016**, *136*, 560–570. [CrossRef]
31. Jia, B.; Liu, F.; Wang, D. Experimental study on the performance of spiral solar air heater. *Sol. Energy* **2019**, *182*, 16–21. [CrossRef]
32. Heydari, A.; Mesgarpour, M. Experimental analysis and numerical modeling of solar air heater with helical flow path. *Sol. Energy* **2018**, *162*, 278–288. [CrossRef]
33. Jiang, Y.; Zhang, H.; Wang, Y.; You, S.; Wu, Z.; Fan, M.; Wang, L.; Wei, S. A comparative study on the performance of a novel triangular solar air collector with tilted transparent cover plate. *Sol. Energy* **2021**, *227*, 224–235. [CrossRef]
34. Singh, S. Thermal performance analysis of semicircular and triangular cross-sectioned duct solar air heaters under external recycle. *J. Energy Storage* **2018**, *20*, 316–336. [CrossRef]
35. Al-Sulttani, A.O.; Ahsan, A.; Al-Bakri, B.A.; Hason, M.M.; Daud, N.N.N.; Idrus, S.; Alawi, O.A.; Macioszek, E.; Yaseen, Z.M. Double-slope solar still productivity based on the number of rubber scraper motions. *Energies* **2022**, *15*, 7881. [CrossRef]
36. Li, L.; Xu, P.; Li, Q.; Zheng, R.; Xu, X.; Wu, J.; He, B.; Bao, J.; Tan, D. A coupled LBM-LES-DEM particle flow modeling for microfluidic chip and ultrasonic-based particle aggregation control method. *Appl. Math. Model.* **2025**, *143*, 116025. [CrossRef]
37. Li, L.; Xu, P.; Li, Q.; Yin, Z.; Zheng, R.; Wu, J.; Bao, J.; Bai, W.; Qi, H.; Tan, D. Multi-field coupling particle flow dynamic behaviors of the microreactor and ultrasonic control method. *Powder Technol.* **2025**, *454*, 120731. [CrossRef]
38. Fu, Z.; Zuo, W.; Li, Q.; Zhou, K.; Huang, Y.; Li, Y. Multi-objective optimization of liquid cooling plate partially filled with porous medium for thermal management of lithium-ion battery pack by RSM, NSGA-II and TOPSIS. *Energy* **2025**, *318*, 134853. [CrossRef]
39. Fu, Z.; Zuo, W.; Li, Q.; Zhou, K.; Huang, Y.; Li, Y. Performance enhancement studies on the liquid cooling plate fully filled with porous medium for thermal management of lithium-ion battery pack. *J. Energy Storage* **2025**, *116*, 116072. [CrossRef]
40. Liu, Z.; Gao, X.; Huang, X.; Xie, Y.; Gao, J.; Yang, X.; He, Q. Evaluation on solar-biogas heating system for buildings: Thermal characteristics and role of heat storage sectors. *Appl. Energy* **2025**, *390*, 125817. [CrossRef]
41. Singh, S.; Dhiman, P. Thermal Performance Analysis of a Rectangular Longitudinal Finned Solar Air Heater with Semicircular Absorber Plate. *J. Sol. Energy Eng.* **2016**, *138*, 011006-9. [CrossRef]
42. Bhattacharya, A.; Mahajan, R.L. Metal Foam and Finned Metal Foam Heat Sinks for Electronics Cooling in Buoyancy-Induced Convection. *J. Electron. Packag.* **2006**, *128*, 259–266. [CrossRef]
43. Bergman, T.L.; Lavine, A.S.; Incropera, F.P.; Dewitt, D.P. *Fundamentals of Heat and Mass Transfer*, 7th ed.; John Wiley & Sons: Hoboken, NJ, USA, 2011.
44. De Lemos, M.J. *Turbulence in Porous Media: Modeling and Applications*; Elsevier: Amsterdam, The Netherlands, 2012.
45. Bejan, A.; Nield, D.A. *Convection in Porous Media*, 5th ed.; Springer: Berlin/Heidelberg, Germany, 2017.
46. Salim, B.; Abdenour, S.; Oualid, C.; Marwani, H.M.; Sami, R.; Aljuraide, N.I.; Althomali, R.H.; Rahman, M.M.; Ali, M.M.; El Bouz, M.A. Three-dimensional transient CFD modeling of multiple finned aluminum foam heat sinks in a horizontal channel. *Alex. Eng. J.* **2023**, *78*, 426–437. [CrossRef]
47. Kalogirou, S.A. *Solar Energy Engineering: Processes and Systems*; Elsevier: Amsterdam, The Netherlands, 2023.
48. Chamoli, S.; Lu, R.; Chen, H.; Cheng, Y.; Yu, P. Numerical optimization of design parameters for a modified double-layer microchannel heat sink. *Int. J. Heat Mass Transf.* **2019**, *138*, 373–389. [CrossRef]

Disclaimer/Publisher's Note: The statements, opinions and data contained in all publications are solely those of the individual author(s) and contributor(s) and not of MDPI and/or the editor(s). MDPI and/or the editor(s) disclaim responsibility for any injury to people or property resulting from any ideas, methods, instructions or products referred to in the content.